

On-chip single-pump interferometric Josephson isolator for quantum measurements

Baleegh Abdo,¹ Oblesh Jinka,¹ Nicholas T. Bronn,¹ Salvatore Olivadese,¹ and Markus Brink¹

¹*IBM Quantum, Yorktown Heights, New York 10598, USA.*

(Dated: November 9, 2021)

Nonreciprocal microwave devices, such as circulators and isolators, are critical in high-fidelity qubit readout schemes. They unidirectionally route the readout signals and protect the qubits against noise coming from the output chain. However, cryogenic circulators and isolators are prohibitive in scalable superconducting architectures because they rely on magneto-optical effects. Here, we realize an on-chip, single-microwave-pump Josephson ISolator (JIS), formed by coupling two nondegenerate Josephson mixers in an interferometric scheme. We unravel the interplay between the orientation parity of the magnetic fluxes, biasing the mixers, and the JIS directionality. Furthermore, we build a motherboard, which integrates the JIS and other superconducting components, including a Josephson directional amplifier, into a printed circuit and use it to read out a qubit with 92% fidelity, while maintaining 75% of its T_{2E} . Improved versions of this motherboard could replace magnetic circulators and isolators in large superconducting quantum processors.

Introduction

Nonreciprocity breaks the transmission-coefficient symmetry for light upon exchanging sources and detectors. A common method for breaking reciprocity is guiding light through magnetic materials exhibiting magneto-optical effects, such as the Faraday effect [1, 2]. Other nonreciprocity schemes include operating in the non-linear regime [3], employing the quantum Hall effect [4–6], and parametrically modulating a certain physical property of the system [7–12].

Due to their ability to break the transmission symmetry, nonreciprocal devices play critical roles in a variety of basic science and technology applications, requiring, for example, signal transport control, separation of input from output in reflective or communication setups, and source protection against backscatter or detector backaction. In particular, in the realm of superconducting quantum processors, nonreciprocal microwave devices, such as circulators and isolators, are critical for performing high-fidelity quantum nondemolition (QND) measurements [13–18]. With relatively low loss, they route readout signals to and from quantum processors in a directional manner and protect qubits against noise coming from the output chain. However, state-of-the-art cryogenic circulators and isolators are prohibitive in scalable architectures because they are bulky and rely on magnetic materials and strong magnetic fields [19, 20], which are difficult to integrate on chip and incompatible with superconducting circuits.

In an attempt to solve this scalability challenge, a variety of viable alternative circulator and isolator schemes have been proposed and realized, which use photonic transitions between coupled resonance modes [21, 22], the Hall-effect [6], frequency conversion in nonlinear transmission lines [23], frequency conversion combined with delay lines [24, 25], dynamical modulation of transfer switches incorporated with delay lines [26], and reservoir engineered optomechanical interactions [27–29]. Here, we realize an on-chip Josephson-based isolator that is compatible with superconducting circuits, devoid of magnetic materials and strong magnets, and, most im-

portantly, can be operated using a single microwave drive. Furthermore, we build a printed circuit motherboard that incorporates such Josephson isolators with other superconducting microwave components, including a Josephson directional amplifier (JDA) [30, 31], and use it to perform high-fidelity qubit measurements, while maintaining a high coherence. Such a motherboard could potentially replace the magnetic circulators and isolators that we use at present in high-fidelity measurement setups and constitute a key component in scalable readout architectures.

The interferometric Josephson isolator (JIS) realized here is based on the isolation scheme recently introduced by our group [32]. It is formed by coupling two nominally identical nondegenerate Josephson mixers [33] via their respective distinct spatial and spectral eigenmodes ‘a’ and ‘b’. One mode in this scheme, e.g. ‘a’, supports input and output propagating signals within the device bandwidth, while the other, e.g., ‘b’, serves as an internal mode of the system coupled to a dissipation port. By parametrically modulating the inductive coupling between the modes, an artificial gauge-invariant potential for microwave photons is generated, which imprints nonreciprocal phase shifts on the transmitted signals through the mixers, undergoing frequency conversion. By further embedding the mixers in an interferometric setup, a unidirectional transmission of propagating signals is created owing to constructive and destructive wave-interference taking place between different paths in the device.

However, unlike the proof-of-principle device presented in Ref. [32], which (1) integrates on-chip superconducting and off-chip normal-metal circuits, and (2) requires, for its operation, two same-frequency phase-locked microwave drives injected through two input lines in the dilution fridge, the present JIS is a superconducting on-chip device that is operated by a single microwave drive fed through one input line. These changes lead to several key advantages, for example, (1) eliminating the losses in the normal metal parts, (2) paving the way for size reduction using lumped-element designs, and (3) requiring only one microwave source and input line on a par

with Josephson parametric amplifiers. The latter leads to savings in the hardware resources required per qubit, easier tune-up procedures, enhanced stability over time, and simpler control circuitry. Understandably, these gains are even more pronounced when comparing this single-pump device with nonreciprocal schemes, which require multiple pumps [11, 21, 22].

Results

Isolators, whose circuit symbol is shown in Fig. 1a, are two-port microwave devices, which transmit microwave signals propagating in the direction of the arrow, i.e., from port 1 to 2, at frequency f_1 (within the device bandwidth), while blocking signals propagating in the opposite direction. Here, we realize an on-chip superconducting JIS that requires a single pump for its operation, as illustrated in Fig. 1b,c. The basic building block of the device, whose photos are shown in Fig. 1e,f, is the Josephson parametric converter (JPC) [33–36], which functions as a lossless nondegenerate three-wave mixing device. The JPC, as illustrated in Fig. 1g, is comprised of two half-wavelength, microstrip resonators denoted ‘a’ and ‘b’, which intersect in the middle at an inductively-shunted Josephson ring modulator (JRM) [37], serving as a dispersive nonlinear medium. The resonators are characterized by flux-tunable resonance frequencies $\omega_{a,b}(\Phi_{\text{ext}})/2\pi$, where Φ_{ext} is the external magnetic flux threading the JRM loop, and bandwidths $\gamma_{a,b}/2\pi$ set by the capacitive coupling to the external feedlines. As illustrated in Fig. 1g, resonator ‘a’ is open ended and has one feedline, resonator ‘b’ has one feedline on each side, and the pump drive is fed to the device via a separate on-chip feedline (marked P). The three-wave mixing operation of the JPC is captured by the leading nonlinear term in the system Hamiltonian given by $\mathcal{H}_{3\text{wave}} = \hbar g_3 (a + a^\dagger)(b + b^\dagger)(c + c^\dagger)$ [33], where g_3 is a flux-dependent coupling strength, a and b are the annihilation operators for the differential modes a and b , while c is the annihilation operator for mode c common to both resonators. When applying a strong, coherent, off-resonant, common drive at $\omega_c \equiv \omega_p = \omega_b - \omega_a$, the JPC acts as a lossless frequency converter between modes a and b [33, 38, 39]. Under this classical drive, we obtain in the rotating wave approximation $\mathcal{H}_{3\text{wave}} = \hbar |g_{ab}| (e^{i\phi'_p} a b^\dagger + e^{-i\phi'_p} a^\dagger b)$, where g_{ab} is a pump-amplitude-dependent coupling strength ($\propto g_3$), and ϕ'_p is a generalized pump phase, which is related to the applied pump phase ϕ_p by $\phi'_p = \phi_p + n_g \pi$, where

$$n_g = \begin{cases} 0 & \varphi_{\text{ext}} \leq 0 \\ 1 & \varphi_{\text{ext}} > 0 \end{cases}. \quad (1)$$

The added phase 0 ($n_g = 0$) or π ($n_g = 1$), depends on whether g_3 is positive or negative, respectively, which is determined by the sign of $\varphi_{\text{ext}} = 2\pi\Phi_{\text{ext}}/\Phi_0$, where $\Phi_0 = h/2e$ is the flux quantum or alternatively the dc-current circulating in it. Equation (1) assumes that the JPCs are flux-biased at the primary flux lobe centered around zero flux.

On resonance, the transmission amplitude associated with the frequency conversion process is given by $t = 2\rho/(1 + \rho^2)$, where $\rho = 2|g_{ab}|/\sqrt{\gamma_a\gamma_b}$ is a dimensionless pump amplitude, which varies between 0 (total reflection) and 1 (full conversion).

As seen in the block diagram of Fig. 1d, the JIS is formed by coupling two nominally identical JPCs in an interferometric setup, where mode ‘a’ of the JPCs is coupled via a 90° hybrid, and mode ‘b’ is coupled to external 50 Ohm cold terminations and an intermediate transmission line (TL). The device also includes a 90° hybrid for the pump that is connected to the pump feedlines of the JPCs. Since this hybrid splits the pump evenly between the two stages and imposes, by design, the required phase difference for nonreciprocity, i.e., $\pm\pi/2$, the device can be powered using a single drive.

Assuming symmetric coupling of mode ‘b’ to the two feedlines, the transmission parameters of the JIS on resonance are given by (see Supplementary Note 1)

$$S_{2\leftarrow 1} = i \frac{\sqrt{1-t^2} \mp \sqrt{2}t^2 \sin(\varphi)}{1+t^2}, \quad (2)$$

and the reflection parameters read

$$S_{11} = S_{22} = -i \frac{\sqrt{2}t^2 \cos(\varphi)}{1+t^2}, \quad (3)$$

where $\varphi \equiv \varphi_p + p\pi$, $\varphi_p \equiv \phi_{p1} - \phi_{p2}$ is the phase difference between the same-frequency pumps feeding the two stages and $p \equiv (n_{g1} + n_{g2}) \bmod 2$ is the parity of the applied fluxes threading the two JRMs.

From these definitions and Eq. (1), it follows that $\varphi_p = \mp\pi/2$ when ports P₁ and P₂ are driven, respectively, and $p = 0$ when the signs of $\varphi_{\text{ext}1}$ and $\varphi_{\text{ext}2}$ are the same, i.e., even parity, and $p = 1$ when their signs are opposite, i.e., odd parity (for further details see Supplementary Notes 1-3).

By operating the two JPCs in frequency conversion mode at the 50:50 beam splitting point, i.e., $t = 1/\sqrt{2}$, in which half of the signal input on each port is reflected and half is transmitted with frequency conversion to the other port (as illustrated in the signal flow graph in Fig. 1h), and by setting, for example, the generalized phase difference to $\varphi = \varphi_p = -\pi/2$, attained in the case of pumping through P₁ while $p = 0$, we generate a nonreciprocal response, in which input signals on resonance propagating in the direction of the arrow shown in Fig. 1b, are transmitted with near unity transmission, i.e., $|S_{21}| = 2\sqrt{2}/3 \simeq 0.94$ (equivalent to about 0.5 dB loss in signal power), whereas signals propagating in the opposite direction are blocked $S_{12} = 0$ (i.e., routed to the cold terminations), and reflections vanish $S_{11} = S_{22} = 0$.

Figure 2 exhibits a measurement of the scattering parameters of the JIS operated in two modes of operation at fixed applied fluxes, for which $p = 0$. In the first, the JIS is driven through P₁, setting its directionality from port 1 to 2, while in the second, it is driven

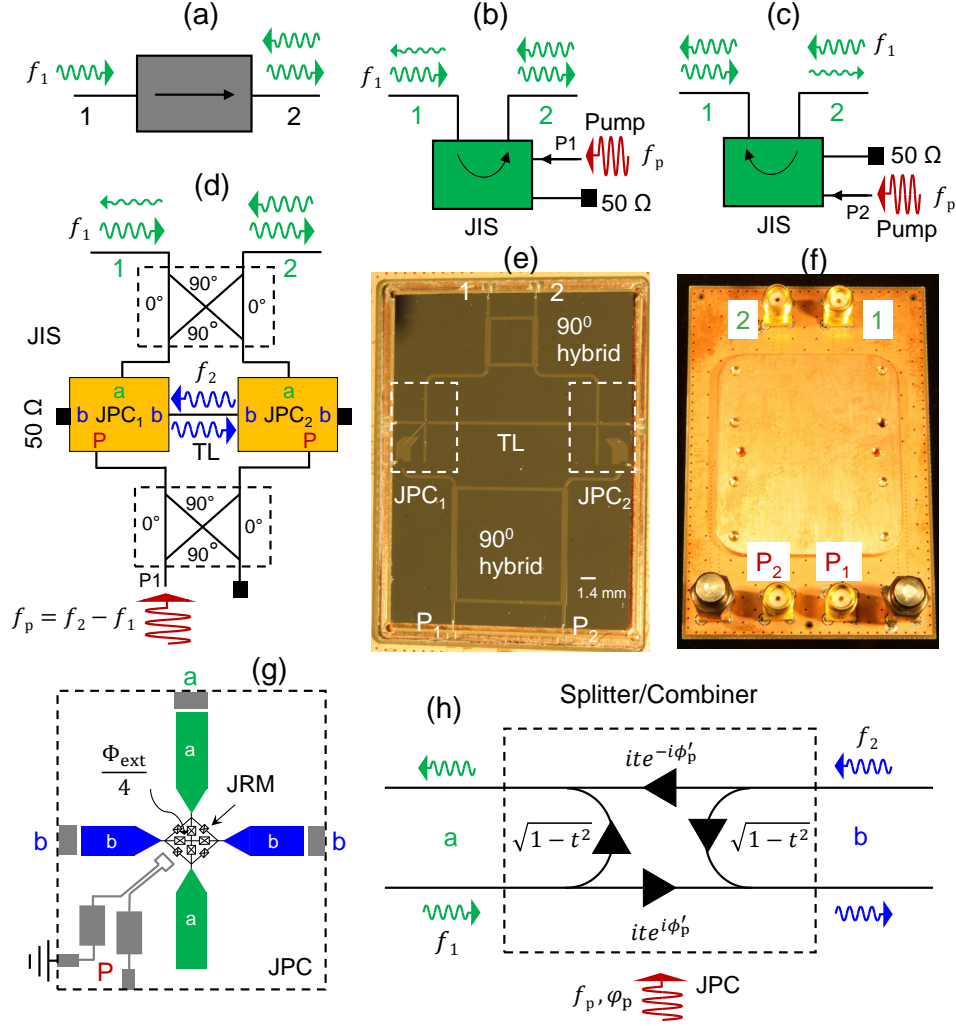


FIG. 1: **On-chip single-pump interferometric Josephson Isolator (JIS).** **a** Isolator circuit symbol. In an ideal isolator, input signals propagating in the direction of the arrow are fully transmitted; signals propagating in the opposite direction are blocked. **b** and **c** circuit symbols for the JIS. The direction of the arrow depends on which pump port of the device is driven. **d** A block diagram of the JIS scheme. It consists of two identical JPCs coupled in an interferometric setup. **e** Photo of the JIS chip. The two JPCs, the signal hybrid, the coupling transmission line (TL), and the pump hybrid are all superconducting and realized on the same chip. **f** Photo of the PCB and bottom cover of the JIS. The length and width of the PCB are 7.62 cm and 5.08 cm, respectively. **g** JPC design used in the JIS. **h** Signal flow graph of the JPC operated in frequency conversion mode without photon gain. Signals impinging on ports ‘a’ and ‘b’ undergo frequency conversion and transmission to the other port with amplitude t and get reflected off with amplitude $\sqrt{1-t^2}$. The transmitted signal acquires a nonreciprocal phase shift $\pm\phi'_p$, where ϕ'_p is the generalized pump phase.

through P_2 , which reverses its directionality as illustrated in the block diagrams in the left column. In Fig. 2a, we show the transmission parameters $|S_{21}|^2$ (blue) and $|S_{12}|^2$ (orange) corresponding to the first case. The dashed and solid lines correspond to the JIS being off (no pump) and on (with pump), respectively. Similarly, Fig. 2c, exhibits the reversed transmission response corresponding to the second case. In both cases, the JIS response yields on resonance at 6.84 GHz about 2 dB attenuation in the forward direction and 23 dB in the backward (isolated)

direction with a dynamical bandwidth of 8 MHz. Figures 2b,d depict the reflection parameters S_{11} (red) and S_{22} (magenta) measured for the respective directionality cases. As seen in Figs. 2b,d the reflections off the two ports are small when the pump is on and off, depicted as solid and dashed lines, respectively. In addition to demonstrating that the on-chip single-pump JIS works as intended, the results of Fig. 2 directly confirm the theory prediction that the phase gradient condition for nonreciprocity is $\pm\pi/2$ because these are the phase differ-

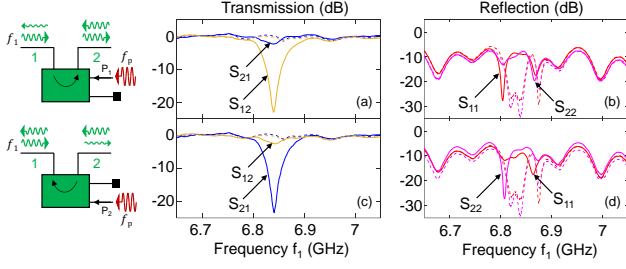


FIG. 2: **Measured scattering parameters of the JIS.** **a** and **b** display transmission parameters, i.e., $|S_{21}|^2$ (blue), $|S_{12}|^2$ (orange) and reflection parameters, i.e., $|S_{11}|^2$ (red), $|S_{22}|^2$ (magenta) measured versus signal frequency for a pump applied to P_1 at $f_p = 2.758$ GHz. The solid and dashed curves correspond to pump on and off, respectively. **c** and **d** are the same as **a** and **b**, except that the pump is applied to P_2 instead.

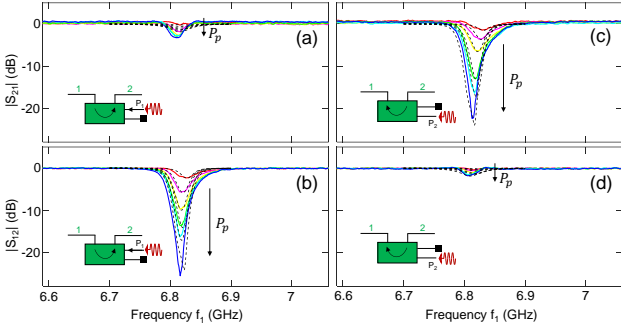


FIG. 3: **JIS transmission versus pump power.** Transmission parameters measured versus signal frequency for varying pump powers applied at $f_p = 2.727$ GHz. **a** and **b** exhibit measured transmission parameters $|S_{21}|^2$, $|S_{12}|^2$ versus frequency for varying pump powers applied to P_1 . **c** and **d** are the same as **a** and **b** obtained for varying pump powers applied to P_2 . The black dashed curves represent a calculated response of the JIS. The calculation sequence and the parameters used are included in Supplementary Note 2.

ences imposed by the pump hybrid.

Since the JPCs in the JIS are operated in frequency conversion mode without photon gain, they are not required to add noise to the processed signal [40, 41]. However, any added noise by the JIS is primarily set by its insertion loss in the forward direction, e.g., $|S_{ij}|^2$ (assuming $j \rightarrow i$), and is given by $n_{\text{add}} = (1 - |S_{ij}|^2)/2|S_{ij}|^2$, where n_{add} is the noise-equivalent-input-photons at the signal frequency [32]. For the measurement of Fig. 2, which exhibits about 2 dB attenuation in the forward direction, we get $n_{\text{add}} = 0.29$. In the ideal case scenario, i.e., with 0.5 dB of attenuation, this figure would be much lower $n_{\text{add}} = 0.0625$.

Next, in Fig. 3, we measure, for a fixed pump frequency and fluxes (for which $p = 0$), $|S_{21}|^2$ and $|S_{12}|^2$ of

the JIS, as we vary the pump power. Figures 3a,b show measurements of $|S_{21}|^2$ and $|S_{12}|^2$ when P_1 is driven (i.e., $1 \rightarrow 2$), whereas Figs. 3c,d show measurements of the same transmission parameters when P_2 is driven instead (i.e., $2 \rightarrow 1$). The colored solid curves are measured data, whereas the black dashed curves represent a calculated response of the device using the theory model presented in Supplementary Note 2. As seen in these measurements, the device response varies with the pump power in a monotonic and stable manner similar to the observed response of JPCs [36] and JPAs [42]. Other important characterization and measurement results of the JIS can be found in Supplementary Note 4.

Figure 4 exhibits an important result. It demonstrates that the direction of the transmission/isolation of the device is determined not only by the sign of the phase difference of the pumps feeding the two JPCs but also by the orientation parity of the magnetic fields biasing the two JPCs or alternatively the parity of the circulating currents flowing in the JRM loops, which, in turn, determines the sign of the coupling between the eigenmodes of the JPCs. As seen in the measurement results of Fig. 4, for the same pump feeding the same pump port P_1 or P_2 , the direction of the transmission/isolation can be reversed by flipping the magnetic flux in one JRM loop or preserved by flipping the magnetic flux threading two loops. This result opens the door for magnetic-field detection applications, such as the detection of the orientation parity of weak magnetic sources using simple microwave transmission measurements as outlined in Supplementary Note 5. It is important to point out here that although the parity of the magnetic fields biasing the JPCs plays a role in setting the directionality of the JIS, it does not generate its nonreciprocal response, which is primarily induced by the pump phase difference. It is also important to outline here that such a systematic investigation of the effect of the parity of the applied fluxes on the JIS directionality is made possible owing to the single-pump feature of the device. Without it, pinning down this effect would have been more challenging.

After successfully demonstrating the JIS operation as a standalone device, we now show how it can be integrated with other microwave components to form a motherboard that could replace magnetic circulators and isolators in high-fidelity measurement chains. The layout and photo of the motherboard, shown in Fig. 5a and Fig. 5b, respectively, integrates: a Purcell filter [32, 43], a superconducting wideband directional coupler [32], two JIS devices (sideline: JIS 2 got damaged during wirebonding and, thus, is not operational), and an on-chip JDA. The motherboard has a few pump ports employed for powering the Josephson devices (the JDA requires for its operation two same-frequency pumps, whose phase difference between P_3 and P_4 is $-\pi/2$) and three main ports connecting to the readout input line, the quantum chip, and the readout output line. The output line employed in the experiment includes two wideband, magnetic isolators to protect the quantum system against noise coming

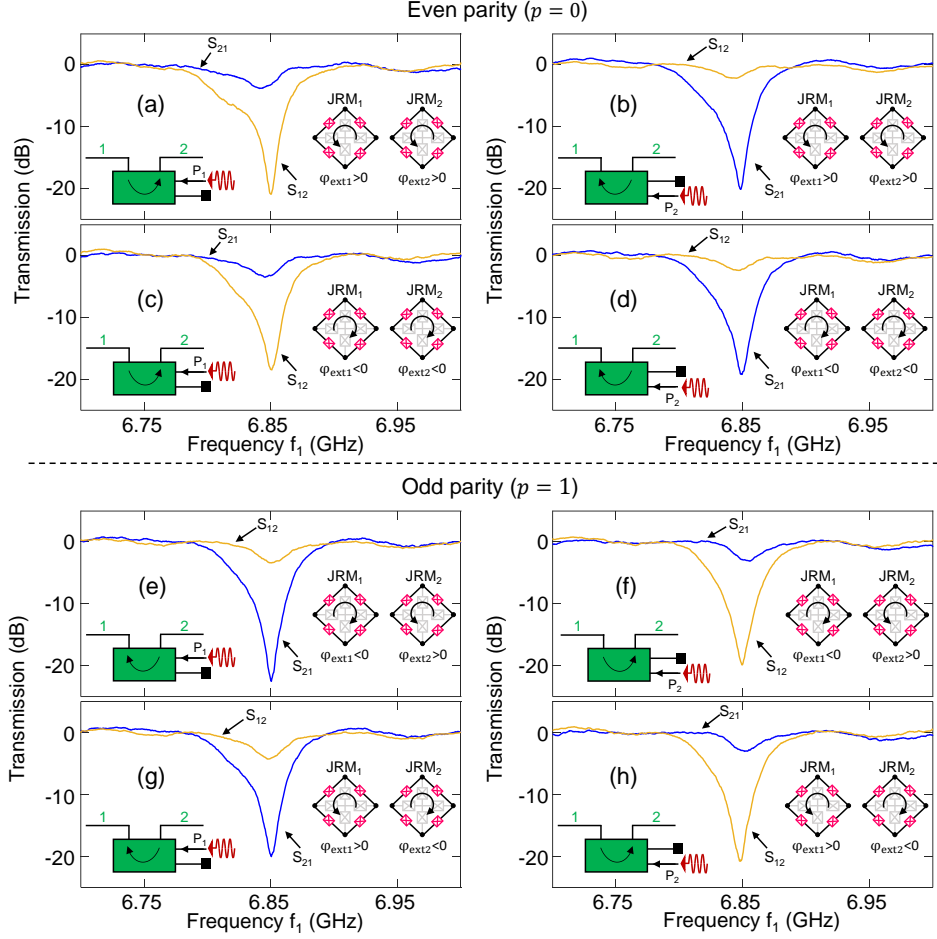


FIG. 4: **Dependence of the transmission/isolation direction on the parity of the fluxes threading the two JRMs.** Transmission parameters of JIS measured versus signal frequency. The measurement results shown in the left (right) column are taken while applying the pump drive to P_1 (P_2) at $f_p = 2.783$ GHz. In the upper half of the figure, representing the even parity cases ($p = 0$), the magnetic fluxes threading the two JRMs are either $\varphi_{\text{ext}1} > 0$, $\varphi_{\text{ext}2} > 0$ in **a** and **b** or $\varphi_{\text{ext}1} < 0$, $\varphi_{\text{ext}2} < 0$ in **c** and **d**. In the bottom half of the figure, representing the odd parity cases ($p = 1$), the magnetic fluxes threading the two JRMs are either $\varphi_{\text{ext}1} < 0$, $\varphi_{\text{ext}2} > 0$ in **e** and **f** or $\varphi_{\text{ext}1} > 0$, $\varphi_{\text{ext}2} < 0$ in **g** and **h**. The magnitude of the flux used is $|\varphi_{\text{ext}1}| = |\varphi_{\text{ext}2}| = 2\pi \cdot 1.12$ (i.e., $\Phi_{\text{ext}} = 1.12\Phi_0$).

from the HEMT amplifier. The necessity of these isolators will be investigated in future work.

When directly coupling this motherboard to a qubit-resonator device, without any intermediate magnetic circulators and isolators, we are able to read out the qubit with high-fidelity, while maintaining a good coherence as demonstrated in Fig. 6. Readout signals input on the directional coupler get attenuated by about 18 dB and transmitted through the Purcell filter to the qubit chip. The reflected readout signal carrying the qubit information is transmitted through the various components of the motherboard and exits via its outport port. Note that in this outward direction the directional coupler does not attenuate the quantum signal, thus, it does not degrade the signal to noise ratio. Microwave measurements of the motherboard in the qubit setup are shown in Methods.

In Fig. 6a, we show the baseline case, in which both JIS 1 and the JDA are off. In this case, the fidelity is 60%, $T_1 = 60 \mu\text{s}$, $T_{2E} = 54 \mu\text{s}$. When JIS 1 is turned on while the JDA is off, shown in Fig. 6b, T_1 and T_{2E} are preserved, whereas the fidelity slightly decreases to 57% due to the added attenuation by the JIS in the forward direction. Next, in Fig. 6c, the JDA is turned on with a gain of 19 dB and the JIS 1 is turned off. In this case, as expected, the fidelity rises significantly to 93%, T_1 decreases slightly to $55 \mu\text{s}$, while T_{2E} drops by a factor of 9 due to excess backaction generated by the JDA. Finally, in Fig. 6d, both JIS 1 and the JDA are turned on. In this case, we achieve a fidelity of 92%, preserve T_1 and maintain 75% of T_{2E} compared to the baseline case in which both Josephson devices are off. Based on the achieved improvement in T_{2E} between configurations c and d, we

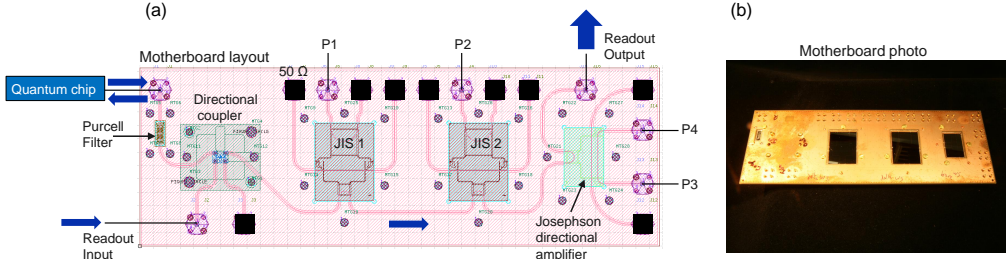


FIG. 5: **Motherboard for high-fidelity readout.** **a** Motherboard layout featuring a printed circuit board which integrates several superconducting microwave components including: a Purcell filter, a superconducting directional coupler, two JIS devices, and a JDA. The motherboard has seven ports, four for feeding the pumps to the Josephson devices, and three main ports that connect to the readout input line, the quantum chip and the readout output line. Other auxiliary ports are terminated by 50 Ohm terminations. **b** Photo of the motherboard. The length and width of the motherboard are 19.69 cm and 6.73 cm, respectively.

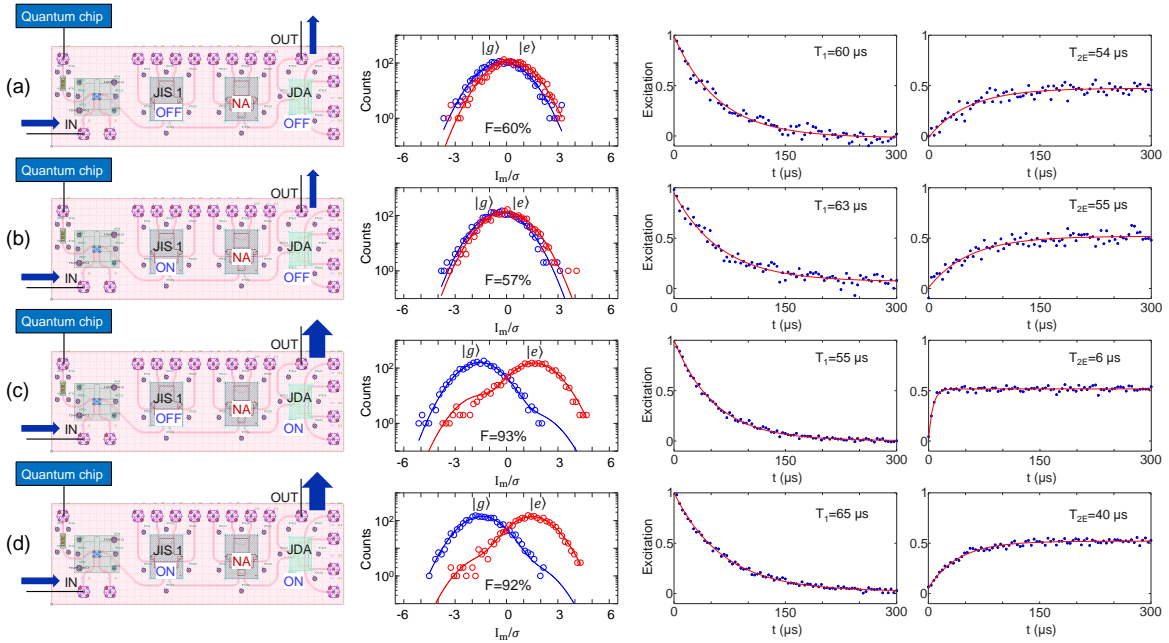


FIG. 6: **High-fidelity qubit readout without intermediate magnetic circulators and isolators.** The columns exhibit, from left to right, motherboard configurations, followed by respective measurements of readout fidelity, T_1 , and T_{2E} . **a** JIS 1 and JDA are off. **b** JIS 1 is on and JDA is off. **c** JIS 1 is off and JDA is on. **d** JIS 1 and JDA are on.

estimate that JIS 1 is providing about 13 dB of isolation in configuration d (see table 1 in Methods). It is worthwhile noting that tuning the JIS in the motherboard is a bit challenging because, unlike amplification, isolation is not observed directly via a transmission measurement between input and output, but indirectly through the protection it provides to the qubit. This technical issue can be resolved in future work by either developing automatic tune-up procedures, which optimize for qubit coherence and readout fidelity as a function of the pump power and frequency, while the JDA is turned on or by using a predetermined lookup table of working point sett-

ings, measured in a separate cooldown, which covers the range of expected readout frequencies.

Discussion

The motherboard-qubit experiment presented in this work differs in three key aspects from the proof-of-principle qubit-JIS experiment introduced in Ref. [32], namely, (1) the JIS realized and employed in this work is an on-chip superconducting device operated with a single pump, whereas the JIS in Ref. [32] is an integrated circuit of normal-metal and superconducting components operated with two pumps, (2) the JIS, the Purcell filter, and the superconducting directional coupler are inte-

grated here into one printed circuit board, whereas in the previous work, they are separate components, connected by hand-formable coax cables, (3) the motherboard integrates a JDA, whereas the previous experiment utilizes a magnetic circulator combined with a JPC amplifying in reflection. In addition to the hardware-saving advantage of eliminating a circulator in the signal path, using a JDA (instead of the JPC) has the important advantage of requiring less total isolation between the qubit and the quantum limited amplifier for the same amplifier gain and qubit dephasing time (assuming the latter is dominated by nonthermal photon shot noise in the readout resonator due to excess amplifier backaction).

Also, the measured response of the JIS shown in Figs. 2, 3 differ from the ideal theoretical case scenario in two notable aspects. The first is that the JIS attenuation on resonance in the forward direction of about 2 dB is higher than the 0.5 dB, predicted for a device, whose JPCs are operated around the 50:50 beamsplitting point, and whose modes ‘b’ are equally coupled to each other and to the cold terminations. The likely cause for this effect, as revealed from the calculated response in Fig. 3, is that modes ‘b’ of the JPCs are coupled more strongly to the cold terminations than to each other (see Supplementary Note 2). Consequently, this suggests it is possible to reduce the forward attenuation of the device by adjusting the unintentional asymmetry in the couplings in future designs. The second is the slight frequency detuning between the dips in the reflection (Fig. 2b,d) and transmission (Fig. 2a,c) parameters when the JIS is on. This effect could be due to a phase imbalance in the signal hybrid, which results in a slightly different frequency condition for constructive/destructive interferences in the two cases.

Following this work, there are several avenues to explore going forward, for example (1) realizing a single-pump, on-chip JDA, which employs an adapted hybrid for the pump in an analogous manner to the single-pump JIS. The pump frequency in the JDA case (i.e., amplification), is the sum of the resonance frequencies of modes ‘a’ and ‘b’, (2) reducing the size of the motherboard components using lumped-element implementations of the JPCs [44] and hybrids [45], and (3) enhancing the bandwidth and saturation power of the JIS and JDA to support multiplexed qubit readout in scalable architectures. This could potentially be achieved by first enhancing the bandwidth and saturation power of JPCs, which constitute the bottleneck. One possible way to enhance the JPC bandwidth is by implementing an impedance matching network between its Josephson junctions and external feedlines, as was successfully demonstrated in the case of single-port Josephson parametric amplifiers [46, 47]. Enhancing the saturation power of JPCs on the other hand, requires getting a better handle on the Kerr and higher order nonlinearities exhibited by the device [48–50], which are dependent on the inductance ratios of the Josephson junctions to the linear inductances inside and outside the ring [49].

Finally, it is important to point out that the motherboard concept introduced here constitutes an interface block between the qubit system and the input and output lines that is modular and versatile, and, therefore, it is not limited to specific superconducting components or readout schemes. For example, the motherboard could potentially serve in the future readout schemes, which rely on single microwave photon detectors [51–53] instead of parametric amplifiers.

In conclusion, we realize and characterize a superconducting, on-chip, interferometric Josephson isolator that requires a single microwave drive for its operation. The isolator is comprised of two nominally identical nondegenerate, three-wave Josephson mixers that are coupled in an interferometric setup and operated in frequency conversion mode. The microwave drive, giving rise to nonreciprocity in the device, is fed through an on-chip quadrature hybrid, which equally splits the drive between the mixers and imposes the required phase difference, i.e., $\pm\pi/2$, between the split drives. The isolator yields on resonance attenuation of about 2 dB in the forward direction and 23 dB in the backward direction with a dynamical bandwidth of 8 MHz. The device has a tunable bandwidth of about 300 MHz with isolation larger than 18 dB and input saturation power of about -120 dBm at 21 dB of isolation (see Supplementary Note 4). We investigate the interplay between the orientation parity of the magnetic fluxes, biasing the mixers, and the isolator directionality. In particular, we show that the JIS directionality can be reversed for the same pump by changing the orientation parity. Such an effect could allow the detection of the orientation parity of pairs of weak magnetic sources using microwave transmission measurements. Moreover, we devise a motherboard that integrates a Purcell filter, a superconducting directional coupler, two JIS devices, and one JDA. By coupling the motherboard to a superconducting qubit without any intermediate stages and turning on the JDA and one JIS, we demonstrate a high-fidelity readout in excess of 90%, while preserving T_1 of the qubit and maintaining 75% of its T_{2E} , compared to the off state of the Josephson devices. An improved and smaller version of this motherboard, which integrates large-bandwidth and high-saturation JIS and JDA devices could enable frequency multiplexed readout of multiple qubits in scalable quantum processor architectures.

Methods

Motherboard characterization

Figure 7, shows a broadband transmission measurement result of the motherboard experiment setup taken using a vector network analyzer. The measurement includes the attenuation of the input line, the transmission of the motherboard, and the amplification of the output line. The main features seen in this measurement result is set by the Purcell filter incorporated into the motherboard, namely the transmission peak plateau seen surrounding the readout frequency and the strong attenuation encompassing the qubit frequency. The locations of these

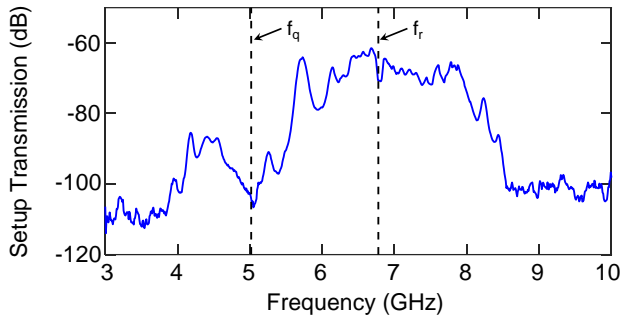


FIG. 7: **Motherboard transmission measurement.** The transmission measurement is taken using a vector network analyzer in the frequency range 3 – 10 GHz. It includes the attenuation of the input line, the transmission of the motherboard, and the amplification of the output line. The black dashed vertical lines indicate the location of the readout and qubit frequencies.

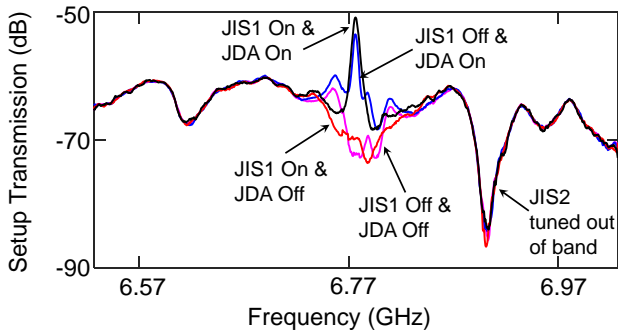


FIG. 8: **Motherboard working point measurement.** The transmission measurement centered around the readout frequency is taken for the motherboard setup. It includes the attenuation of the input line, the transmission of the motherboard, and the amplification of the output line. The curves represent the setup transmission measured for JIS 1 and JDA off (magenta), JIS 1 on and JDA off (red), JIS 1 off and JDA on (blue), JIS 1 and JDA on (black).

two frequencies are indicated using black dashed vertical lines.

In Fig. 8, we depict transmission measurements of the motherboard setup taken at the working point of Fig. 6 near the readout frequency. The measured curves represent the different motherboard configurations corresponding to JIS 1 and the JDA are off (magenta), JIS 1 is on and the JDA is off (red), JIS 1 is off and the JDA is on (blue), and JIS 1 and the JDA are on (black). The large dip appearing on the right side of the figure represents the response of the damaged JIS 2, which is flux-biased outside the measurement bandwidth. It is worth noting that, although the peak of the black curve at the readout frequency is higher than the blue curve,

the JDA gain is fixed and equals to about 19 dB in both cases. This is because the transmission landscape versus frequency slightly changes when JIS 1 is on (red) versus JIS 1 is off (magenta).

Further details about the design, fabrication, packaging, and performance of the Purcell filter and the superconducting directional coupler can be found in Refs.[32, 43].

Qubit measurement parameters

The qubit used in the motherboard experiment is a single Josephson junction transmon capacitively coupled to a superconducting waveguide resonator measured in reflection. The qubit chip has a separate input port through which we control the qubit, which is separate from the readout input line connected to the motherboard. The qubit and readout frequencies are $f_q = 5.0182$ GHz and $f_r = 6.77669$ GHz. The readout resonator bandwidth is $\kappa/2\pi = 1.1$ MHz, while the qubit-state dependent readout frequency shift is $\chi/2\pi = 0.94$ MHz. The readout pulse duration is $T_m = 1$ μ s with an average photon number $\bar{n}_m \simeq 2$. The qubit data is averaged over 2000 iterations. Using the expression $\tan(\theta/2) = \chi/\kappa$, we extract a qubit-state-dependent phase shift of the readout signal $\theta = 81^\circ$. By substituting the histogram peak location $\bar{I}/\sigma = 1.55$ for configuration Fig. 6d (in which the JDA and JIS are on) in the relation $\bar{I}/\sigma = \sqrt{2\bar{n}_m\eta\kappa T_m} \sin(\theta/2)$ [54], we obtain an approximate value for the measurement efficiency of our readout chain $\eta \simeq 0.2$. The forward power gain of the JDA is 19 dB, and its dynamical bandwidth is 6.2 MHz. The frequency of the pumps applied to the JDA and JIS 1 are 16.447 GHz and 2.685 GHz, respectively.

JDA backaction and JIS isolation

Config.	JIS	JDA	T_1 (μ s)	T_{2E} (μ s)	T_ϕ (μ s)	\bar{n}_{th}	\bar{n}_{ba}
a	OFF	OFF	60	54	98	0.003	0
b	ON	OFF	63	55	98	0.003	0
c	OFF	ON	55	6	6.4	0.003	0.04
d	ON	ON	65	40	58	0.003	0.002

TABLE I: **Coherence and backaction comparison.** Evaluated T_ϕ , \bar{n}_{th} , and \bar{n}_{ba} for the different configurations.

In table I, we list the qubit T_1 , T_{2E} , and T_ϕ corresponding to the four motherboard configurations displayed in Fig. 6. The dephasing time T_ϕ is extracted from the measured T_1 and T_{2E} using the relation $1/T_\phi = 1/T_{2E} - 1/2T_1$. Since $T_{2E} < 2T_1$, the qubit coherence time is limited by dephasing. Considering photon shot noise in the resonator mode, which is typically the dominant dephasing mechanism in dispersively-coupled qubit-resonator systems [55–57], the dephasing rate $\Gamma_\phi \equiv 1/T_\phi$ is given by $\Gamma_\phi = \bar{n}\kappa\chi^2/(\kappa^2 + \chi^2)$, where \bar{n} is the average photon number in the resonator, which can be written as $\bar{n} = \bar{n}_{th} + \bar{n}_{ba}$, where \bar{n}_{th} and \bar{n}_{ba} are the average

thermal and nonthermal (backaction) photon numbers, respectively. Using these relations, we evaluate \bar{n}_{th} , and \bar{n}_{ba} for the different configurations of Fig. 6 (see Table I). Note that in table I, we assume that \bar{n}_{th} does not vary in the various configurations and that the excess dephasing is caused by excess JDA backaction in the form of amplified noise leaking into the readout resonator, as a result

of insufficient isolation (backaction photons). Since \bar{n}_{ba} is reduced by a factor of 20 between configurations **c** (JIS off) and **d** (JIS on) while the JDA is on, we estimate the JIS isolation to be about 13 dB.

Data Availability The data that support the findings of this study are available from the corresponding author upon reasonable request.

-
- [1] Hogan, C. L. The ferromagnetic Faraday effect at microwave frequencies and its applications. *Rev. Mod. Phys.* **25**, 253262 (1953).
- [2] Caloz, C. et al. Electromagnetic nonreciprocity. *Phys. Rev. Appl.* **10**, 47001 (2018).
- [3] Fan, L. et al. An all-silicon passive optical diode. *Science* **335**, 447 (2012).
- [4] Viola, G. & DiVincenzo, D. P. Hall effect gyrators and circulators. *Phys. Rev. X* **4**, 021019 (2014).
- [5] Bosco, S., Haupt, F., DiVincenzo, D. P. self-impedance-matched Hall-effect gyrators and circulators. *Phys. Rev. Applied* **7**, 024030 (2017).
- [6] Mahoney, A.C. et al. On-chip microwave quantum Hall circulator. *Phys. Rev. X* **7**, 011007 (2017).
- [7] Fang, K., Yu, Z. & Fan, S. Photonic Aharonov-Bohm Effect based on dynamic modulation. *Phys. Rev. Lett.* **108**, 153901 (2012).
- [8] Fang, K., Yu, Z. & Fan, S. Experimental demonstration of a photonic Aharonov-Bohm effect at radio frequencies. *Phys. Rev. B* **87**, 060301(R) (2013).
- [9] Galland, C., Ding, R., Harris, N. C., Baehr-Jones, T. & Hochberg, M. Broadband on-chip optical non-reciprocity using phase modulators. *Opt. Express* **21**, 14500 (2013).
- [10] Kerckhoff, J., Lalumire, K., Chapman, B. J., Blais, A. & Lehnert, K.W. On-chip superconducting microwave circulator from synthetic rotation. *Phys. Rev. Applied* **4**, 034002 (2015).
- [11] Ranzani, L. & Aumentado, J. Graph-based analysis of nonreciprocity in coupled-mode systems. *New J. of Phys.* **17**, 023024 (2015).
- [12] Kamal, A., Clarke, J. & Devoret, M. Noiseless nonreciprocity in a parametric active device. *Nat. Phys.* **7**, 311 (2011).
- [13] Devoret, M. H. & Schoelkopf, R. J. Superconducting circuits for quantum information: An Outlook. *Science* **339**, 1169 (2013).
- [14] Vijay, R., Slichter, D. H. & Siddiqi, I. Observation of quantum jumps in a superconducting artificial atom. *Phys. Rev. Lett.* **106**, 110502 (2011).
- [15] Ristè, D., Leeuwen, J. G., Ku, H.-S., Lehnert, K. W. & DiCarlo, L. Initialization by measurement of a superconducting quantum bit circuit. *Phys. Rev. Lett.* **109**, 050507 (2012).
- [16] Campagne-Ibarcq, P. et al. Persistent control of a superconducting qubit by stroboscopic measurement feedback. *Phys. Rev. X* **3**, 021008 (2013).
- [17] Sun, L. et al. Tracking photon jumps with repeated quantum non-demolition parity measurements. *Nature* **511**, 444 (2014).
- [18] Ofek, N. et al. Extending the lifetime of a quantum bit with error correction in superconducting circuits, *Nature* **536**, 441 (2016).
- [19] Pozar, D. M. *Microwave Engineering*. 3rd edn (Wiley, Hoboken, 2005).
- [20] Collin, R. E. *Foundations for Microwave Engineering* 2nd edn (Wiley-Interscience, Hoboken, 2014).
- [21] Sliwa, K. et al. Reconfigurable Josephson circulator/directional amplifier. *Phys. Rev. X* **5**, 041020 (2015).
- [22] Lecocq, F. et al. Nonreciprocal microwave signal processing with a field-programmable Josephson amplifier. *Phys. Rev. Applied* **7**, 024028 (2017).
- [23] Ranzani, L. et al. Wideband isolation by frequency conversion in a Josephson-junction transmission line. *Phys. Rev. Applied* **8**, 054035 (2017).
- [24] Chapman B. J. et al. Widely tunable on-chip microwave circulator for superconducting quantum circuits. *Phys. Rev. X* **7**, 041043 (2017).
- [25] Eric I. Rosenthal, E. I., Chapman B. J., Higginbotham, A. P., Kerckhoff, J. & Lehnert K.W. Breaking Lorentz reciprocity with frequency conversion and delay. *Phys. Rev. Lett.* **119**, 147703 (2017).
- [26] Chapman, B. J. Rosenthal, E. I. & Lehnert, K. W. Design of an on-chip superconducting microwave circulator with octave bandwidth. *Phys. Rev. Applied* **11**, 044048 (2019).
- [27] Bernier, N. R. et al. Nonreciprocal reconfigurable microwave optomechanical circuit. *Nat. Commun.* **8**, 604 (2017).
- [28] Barzanjeh, S. et al. Mechanical on-chip microwave circulator. *Nat. Commun.* **8**, 953 (2017).
- [29] Metelmann, A. & Clerk, A.A. Nonreciprocal photon transmission and amplification via reservoir engineering. *Phys. Rev. X* **5**, 021025 (2015).
- [30] Abdo, B. et al. Multi-path interferometric Josephson directional amplifier for qubit readout. *Quantum Sci. Technol.* **3**, 024003 (2018).
- [31] Abdo, B. et al. Josephson directional amplifier for quantum measurement of superconducting circuits. *Phys. Rev. Lett.* **112**, 167701 (2014).
- [32] Abdo, B. et al., Active protection of a superconducting qubit with an interferometric Josephson isolator. *Nat. Commun.* **10**, 3154 (2019).
- [33] Abdo, B., Kamal, A. and Devoret, M. H. Nondegenerate three-wave mixing with the Josephson ring modulator. *Phys. Rev. B* **87**, 014508 (2013).
- [34] Abdo, B., Chavez-Garcia, J. M., Brink, M., Keefe, G. and Chow, J. M. Time-multiplexed amplification in a hybridless and coil-less Josephson parametric converter. *Appl. Phys. Lett.* **110**, 082601 (2017).
- [35] Abdo, B., Schackert, F., Hatridge, M., Rigetti, C. and Devoret, M. Josephson amplifier for qubit readout. *Appl. Phys. Lett.* **99**, 162506 (2011).
- [36] Bergeal, N. et al. Phase-preserving amplification near the quantum limit with a Josephson ring modulator. *Nature* **465**, 64 (2010).

- [37] Roch, N. et al. Widely tunable, nondegenerate three-wave mixing microwave device operating near the quantum limit. *Phys. Rev. Lett.* **108**, 147701 (2012).
- [38] Abdo, B. et al. Full coherent frequency conversion between two propagating microwave modes. *Phys. Rev. Lett.* **110**, 173902 (2013).
- [39] Flurin, E., Roch, N., Pillet, J.D., Mallet, F. and Huard, B. Superconducting quantum node for entanglement and storage of microwave radiation. *Phys. Rev. Lett.* **114**, 090503 (2015).
- [40] Caves, C. M. Quantum limits on noise in linear amplifiers. *Phys. Rev. D* **26**, 1817 (1982).
- [41] Clerk, A. A., Devoret, M. H., Girvin, S. M., Marquardt, F. and Schoelkopf, R. J. Introduction to quantum noise, measurement, and amplification. *Rev. Mod. Phys.* **82**, 1155 (2010).
- [42] Zhou, X. et al. High-gain weakly nonlinear flux-modulated Josephson parametric amplifier using a SQUID array. *Phys. Rev. B* **89**, 214517 (2014).
- [43] Bronn, N. T. et al. Broadband filters for abatement of spontaneous emission in circuit quantum electrodynamics. *Appl. Phys. Lett.* **107**, 172601 (2015).
- [44] Pillet, J.-D., Flurin, E., Mallet, F. and Huard, B. A compact design for the Josephson mixer: The lumped element circuit. *Appl. Phys. Lett.* **106**, 222603 (2015).
- [45] Lu, L.-H. et al. Design and implementation of micro-machined lumped quadrature (90°) hybrids, Microwave Symposium Digest. *IEEE MTT-S International* **2**, 1285 (2001).
- [46] Roy, T. et al. Broadband parametric amplification with impedance engineering: Beyond the gain-bandwidth product. *Appl. Phys. Lett.* **107**, 262601 (2015).
- [47] Mutus, J. et al. Strong environmental coupling in a Josephson parametric amplifier. *Appl. Phys. Lett.* **104**, 263513 (2014).
- [48] Liu, G. et al. Josephson parametric converter saturation and higher order effects. *Appl. Phys. Lett.* **111**, 202603 (2017).
- [49] Liu, C., Chien, T.-C., Hatridge, M. & Pekker D. Optimizing Josephson-ring-modulator-based Josephson parametric amplifiers via full Hamiltonian control. Preprint at <https://arxiv.org/abs/1911.11176v1> (2019).
- [50] Planat, L. et al. Understanding the saturation power of Josephson parametric amplifiers made from SQUID arrays. *Phys. Rev. Applied* **11**, 034014 (2019).
- [51] Chen, Y.-F. et al. Microwave photon counter based on Josephson junctions. *Phys. Rev. Lett.* **107**, 217401 (2011).
- [52] Govia, L. C. G. et al. High-fidelity qubit measurement with a microwave-photon counter. *Phys. Rev. A* **90**, 062307 (2014).
- [53] Dassonneville, R., Assouly, R., Peronnin, T., Rouchon, P. & Huard, B. Number-resolved photon-counter for propagating microwave mode. Preprint at <https://arxiv.org/abs/2004.05114v1> (2020).
- [54] Hatridge, M. et al. Quantum back-action of an individual variable-strength measurement. *Science* **339**, 178 (2013).
- [55] Sears, A. P. et al. Photon shot noise dephasing in the strong-dispersive limit of circuit QED. *Phys. Rev. B* **86**, 180504(R) (2012).
- [56] Rigetti, C. et al. Superconducting qubit in a waveguide cavity with a coherence time approaching 0.1 ms. *Phys. Rev. B* **86**, 100506(R) (2012).
- [57] Wang, Z. et al. Cavity Attenuators for Superconducting Qubits. *Phys. Rev. Applied* **11**, 014031 (2019).

Acknowledgments B.A. expresses deep gratitude to Jerry M. Chow and Pat Gumann for enabling this work and for their tremendous support. The authors thank the group of David Pappas at NIST for fabricating the directional coupler chip and its package. Work pertaining to the development of the Purcell filter was supported by IARPA under contract W911NF-10-1-0324 and to the development of the pogo-pin packaging by IARPA under contract W911NF-16-1-0114-FE. Contribution of the U.S. Government, not subject to copyright.

Author Contributions B.A. designed the nonreciprocal Josephson devices, performed the experiment, and analyzed the data. N.B. designed the Purcell filter, the PCBs, and the motherboard, O.J. designed the device packages, coils, and mounting brackets, S.O. designed and simulated the directional coupler and the on-chip hybrids. M.B. fabricated the nonreciprocal Josephson devices. B.A. wrote the paper with input and contributions from the other authors.

Competing Interests The authors declare no competing interests.

Supplementary Information for “On-chip single-pump interferometric
Josephson isolator for quantum measurements”

Abdo et al.

arXiv:2006.01918v1 [quant-ph] 2 Jun 2020

Supplementary Note 1: JIS scattering parameters

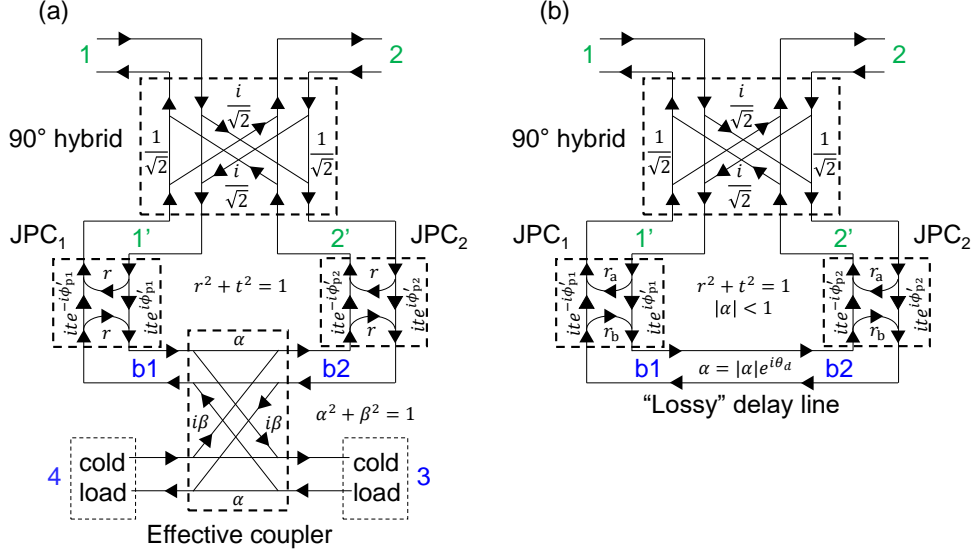
To derive analytical expressions for the scattering parameters of the JIS, we solve the effective signal-flow graph of the device exhibited in Supplementary Figure 1a, which includes the coupled JPCs operated in frequency-conversion mode. On-resonance signals at $f_1 = f_a$ or $f_2 = f_b$ input on port ‘a’ (e.g., 1’ or 2’) or ‘b’ (e.g., b1 or b2) are reflected off with a reflection-parameter r and transmitted with frequency-conversion to the other port with a transmission-parameter t , where r and t are determined by the pump drive amplitude and satisfy the energy conservation condition $r^2 + t^2 = 1$. More specifically, in the stiff pump approximation, r and t can be written as [1, 2]

$$\begin{aligned} r &= \frac{1 - \rho^2}{1 + \rho^2}, \\ t &= \frac{2\rho}{1 + \rho^2}, \end{aligned} \quad (1)$$

where $0 \leq \rho \leq 1$ is a dimensionless pump amplitude. The lower bound $\rho = 0$ corresponds to the case of no applied pump, in which the JPC is off and acts as a perfect mirror, whereas the upper bound $\rho = 1$ corresponds to the case of full frequency conversion mode between ports ‘a’ and ‘b’.

In the derivation, we assume that the two JPCs are balanced, i.e., their reflection and transmission parameters are equal. Supplementary Figure 1a also includes flow-graphs of two couplers coupling the ‘a’ and ‘b’ ports of the JPCs; one represents the 90° hybrid, which couples between the ‘a’ ports of the JPCs, while the other is fictitious, coupling the ‘b’ ports. The latter models the amplitude attenuation α present on the ‘b’ port due to signal absorption in the 50Ω cold loads. Due to the structural symmetry of the device, we consider a coupler with real coefficients α and β , which satisfy the condition $\alpha^2 + \beta^2 = 1$. For an ideal symmetric coupler (i.e., 90° hybrid), $\alpha = \beta = 1/\sqrt{2}$ [3].

A detailed derivation of the scattering parameters of JIS appears in the supplementary information of Ref. [4]. For completeness, we will list in this section the main results of Ref. [4] and update the equations to account for the effect of the applied fluxes in the JRMs on the isolation direction of the JIS. More specifically, we generalize the nonreciprocal phases $\phi_{p1,p2}$ acquired by the frequency-converted transmitted signals between ports ‘a’ and ‘b’, which in Ref. [4] represent only the phases of the pump drives feeding JPC₁ and JPC₂ at frequency f_p , to $\phi'_{p1,p2} = \phi_{p1,p2} + in_g\pi$, which account for the sign of the real coupling constant g_{ab} (i.e., ± 1 obtained for $n_g = 0, 1$, respectively) set by the sign of the applied flux in the JRM or alternatively the direction of the circulating current [5]. Consequently, the multiplication of the transmission parameters through



Supplementary Figure 1: Signal flow graphs for the JIS. The graphs in **a** and **b** exhibit two JPCs operated in frequency conversion mode on resonance, i.e., $f_1 = f_a$, $f_2 = f_b$. Ports ‘a’ of the JPCs, denoted as $1'$, $2'$, are coupled via a 90° hybrid, while their internal ‘b’ ports, denoted as b1 and b2, are coupled via a fictitious coupler in **a** or equivalently a lossy delay line in **b**, which model the attenuation present in the internal ‘b’ channel of the JIS due to dissipation in the 50Ω cold terminations. In **a** the coupler coefficients α and β are taken to be real, satisfying the condition $\alpha^2 + \beta^2 = 1$. The transmitted signals between ports ‘a’ and ‘b’ of the JPC undergo frequency conversion and acquire a nonreciprocal phase shift, which depends on the phase of the drive.

the two JPCs results in multiplication of the signs of the coupling constants or addition of the corresponding phases, i.e., $e^{ip\pi}$ where $p = (n_{g1} + n_{g2}) \bmod 2$. After introducing this update and expressing the JIS scattering parameters in terms of the parameter t , we obtain on resonance

$$S_{21} = \frac{i}{1 + \frac{\alpha^2}{\beta^2} t^2} \left[\sqrt{1 - t^2} - \frac{\alpha}{\beta^2} t^2 \sin \varphi \right], \quad (2)$$

$$S_{12} = \frac{i}{1 + \frac{\alpha^2}{\beta^2} t^2} \left[\sqrt{1 - t^2} + \frac{\alpha}{\beta^2} t^2 \sin \varphi \right], \quad (3)$$

$$S_{11} = S_{22} = -\frac{i\alpha}{\beta^2} \frac{t^2}{1 + \frac{\alpha^2}{\beta^2} t^2} \cos \varphi, \quad (4)$$

$$S_{33} = S_{44} = -\frac{\sqrt{1-t^2}}{1 + \frac{\alpha^2}{\beta^2}t^2}, \quad (5)$$

$$S_{34} = S_{43} = \frac{\alpha}{\beta^2} \frac{t^2}{1 + \frac{\alpha^2}{\beta^2}t^2}, \quad (6)$$

$$S_{13} = -\frac{te^{-i\varphi_s/2+i\pi/4}}{\sqrt{2}\beta \left(1 + \frac{\alpha^2}{\beta^2}t^2\right)} \left[\sqrt{1-t^2}\alpha e^{i\frac{\varphi}{2}+i\frac{\pi}{4}} + e^{-i\frac{\varphi}{2}-i\frac{\pi}{4}} \right], \quad (7)$$

$$S_{14} = -\frac{te^{-i\varphi_s/2+i\pi/4}}{\sqrt{2}\beta \left(1 + \frac{\alpha^2}{\beta^2}t^2\right)} \left[e^{i\frac{\varphi}{2}+i\frac{\pi}{4}} + \sqrt{1-t^2}\alpha e^{-i\frac{\varphi}{2}-i\frac{\pi}{4}} \right], \quad (8)$$

$$S_{23} = -\frac{te^{-i\varphi_s/2+i\pi/4}}{\sqrt{2}\beta \left(1 + \frac{\alpha^2}{\beta^2}t^2\right)} \left[\sqrt{1-t^2}\alpha e^{i\frac{\varphi}{2}-i\frac{\pi}{4}} + e^{-i\frac{\varphi}{2}+i\frac{\pi}{4}} \right], \quad (9)$$

$$S_{24} = -\frac{te^{-i\varphi_s/2+i\pi/4}}{\sqrt{2}\beta \left(1 + \frac{\alpha^2}{\beta^2}t^2\right)} \left[e^{i\frac{\varphi}{2}-i\frac{\pi}{4}} + \sqrt{1-t^2}\alpha e^{-i\frac{\varphi}{2}+i\frac{\pi}{4}} \right], \quad (10)$$

$$S_{31} = -\frac{te^{i\varphi_s/2+i\pi/4}}{\sqrt{2}\beta \left(1 + \frac{\alpha^2}{\beta^2}t^2\right)} \left[\sqrt{1-t^2}\alpha e^{-i\frac{\varphi}{2}+i\frac{\pi}{4}} + e^{i\frac{\varphi}{2}-i\frac{\pi}{4}} \right], \quad (11)$$

$$S_{32} = -\frac{te^{i\varphi_s/2+i\pi/4}}{\sqrt{2}\beta \left(1 + \frac{\alpha^2}{\beta^2}t^2\right)} \left[\sqrt{1-t^2}\alpha e^{-i\frac{\varphi}{2}-i\frac{\pi}{4}} + e^{i\frac{\varphi}{2}+i\frac{\pi}{4}} \right], \quad (12)$$

$$S_{41} = -\frac{te^{i\varphi_s/2+i\pi/4}}{\sqrt{2}\beta \left(1 + \frac{\alpha^2}{\beta^2}t^2\right)} \left[e^{-i\frac{\varphi}{2}+i\frac{\pi}{4}} + \sqrt{1-t^2}\alpha e^{i\frac{\varphi}{2}-i\frac{\pi}{4}} \right], \quad (13)$$

$$S_{42} = -\frac{te^{i\varphi_s/2+i\pi/4}}{\sqrt{2}\beta \left(1 + \frac{\alpha^2}{\beta^2}t^2\right)} \left[e^{-i\frac{\varphi}{2}-i\frac{\pi}{4}} + \sqrt{1-t^2}\alpha e^{i\frac{\varphi}{2}+i\frac{\pi}{4}} \right]. \quad (14)$$

While Eqs. (2)-(14) have the same form as those derived in Ref. [4], the phases φ and φ_s are different. In this case, they are given by $\varphi \equiv \varphi_p + p\pi$ and $\varphi_s \equiv \phi_{p1} + \phi_{p2} + p\pi$, where $\varphi_p = \phi_{p1} - \phi_{p2}$.

Before we outline the effect of the parity parameter p on the JIS response, let us consider two important cases:

1) No applied pump, i.e., $t = 0$. In this case, the scattering matrix reduces into

$$[S] = \begin{pmatrix} 0 & i & 0 & 0 \\ i & 0 & 0 & 0 \\ 0 & 0 & -1 & 0 \\ 0 & 0 & 0 & -1 \end{pmatrix}. \quad (15)$$

This result shows that when the JIS is off, it is transparent for propagating signals and effectively behaves as a lossless transmission line with an added reciprocal phase shift of $\pi/2$ for transmitted signals within the bandwidth of the 90° hybrid.

2) The JPCs are biased at the 50:50 beam splitter working point, i.e., $r = t = 1/\sqrt{2}$, the ‘b’ mode coupler is symmetrical $\alpha = \beta = 1/\sqrt{2}$, the phase difference is $\varphi = -\pi/2$, and the sum is $\varphi_s = \pi/2$. In this case, the scattering matrix becomes

$$[S] = \begin{pmatrix} 0 & 0 & -\frac{1}{\sqrt{2}} & -\frac{1}{\sqrt{2}} \\ \frac{i2\sqrt{2}}{3} & 0 & -\frac{i}{3\sqrt{2}} & \frac{i}{3\sqrt{2}} \\ -\frac{1}{3\sqrt{2}} & -\frac{i}{\sqrt{2}} & -\frac{\sqrt{2}}{3} & \frac{\sqrt{2}}{3} \\ \frac{1}{3\sqrt{2}} & -\frac{i}{\sqrt{2}} & \frac{\sqrt{2}}{3} & -\frac{\sqrt{2}}{3} \end{pmatrix}, \quad (16)$$

which shows that, under the above conditions, the JIS functions as an isolator with almost unity transmission in the forward direction, i.e., $|S_{21}| = 2\sqrt{2}/3 \cong 0.943$ (which corresponds to an insertion loss of about 0.5 dB in the signal power), total isolation in the opposite direction $|S_{12}| = 0$, and vanishing reflections $|S_{11}| = |S_{22}| = 0$. Furthermore, it shows that the cold loads on ports 3 and 4 play a similar role to internal ports of standard magnetic isolators. They dissipate the energy of back-propagating signals $|S_{32}| = |S_{42}| = 1/\sqrt{2}$ and emit noise (e.g., vacuum noise) towards the input $|S_{13}| = |S_{14}| = 1/\sqrt{2}$.

Although Eqs. (2)-(14) are derived for on-resonance signals, it is straightforward to generalize them for signals that lie within the JPC dynamical bandwidth. This is done by substituting [1]

$$t[\omega_1] = \frac{2\rho}{\chi_a^{-1}\chi_b^{-1} + \rho^2}, \quad (17)$$

where χ' s are the bare response functions of modes a and b (whose inverses depend linearly on f_1 and f_2):

$$\begin{aligned}\chi_a^{-1}[\omega_1] &= 1 - 2i \frac{\omega_1 - \omega_a}{\gamma_a}, \\ \chi_b^{-1}[\omega_1] &= 1 - 2i \frac{\omega_1 - \omega_a}{\gamma_b},\end{aligned}\tag{18}$$

where $\omega_1 = 2\pi f_1$, $\omega_a = 2\pi f_a$ and the applied pump angular frequency is given by $\omega_p = \omega_b - \omega_a = \omega_2 - \omega_1$, where $\omega_b = 2\pi f_b$ and $\omega_2 = 2\pi f_2$.

This generalization holds under the assumption that the bandwidth of the 90° hybrid is much larger than the 3 – 12 MHz dynamical bandwidths of the JPCs, which is generally the case because transmission-line-based hybrids typically exhibit bandwidths of a few hundreds of megahertz [6].

Supplementary Note 2: Effective two-port model

Here, we derive an effective two-port model of JIS, which calculates the scattering parameters of ports 1 and 2 only. In this model, we replace the effective coupler shown in Supplementary Figure 1a by a lossy delay line, coupling mode ‘b’ of the two JPCs as depicted in Supplementary Figure 1b. The transmission coefficient of this delay line is frequency dependent and can be expressed as $\alpha[\omega_1] = |\alpha|e^{i\theta_d}$ where the phase delay reads $\theta_d[\omega_1] = \omega_2\sqrt{\epsilon_{\text{eff}}}l_d/c = (\omega_1 + \omega_p)\sqrt{\epsilon_{\text{eff}}}l_d/c$, $l_d = 11.283 \mu\text{m}$ is the length of the microstrip transmission line coupling the two JPCs, c is the speed of light, $\epsilon_{\text{eff}} = 7.418$ is the effective dielectric constant of the microstrip transmission line. The amplitude $0 \leq |\alpha| \leq 1$ represents the amplitude attenuation of the internal mode ‘b’ due to coupling to the cold terminations.

To calculate the device scattering parameters at ports 1 and 2, we start off by writing the scattering parameters of the inner device defined by ports 1’ and 2’, which excludes the 90° hybrid. Using the signal flow graph shown in Supplementary Figure 1b, we obtain

$$s_{1'2'}[\omega_1] = -\frac{\alpha t^2 e^{-i\varphi}}{1 - r_b^2 \alpha^2},\tag{19}$$

$$s_{2'1'}[\omega_1] = -\frac{\alpha t^2 e^{i\varphi}}{1 - r_b^2 \alpha^2},\tag{20}$$

$$s_{1'1'}[\omega_1] = s_{2'2'}[\omega_1] = r_a - \frac{r_b \alpha^2 t^2}{1 - r_b^2 \alpha^2},\tag{21}$$

where the JPC transmission coefficient is given by Eq.(17), r_a and r_b are the JPC reflection parameters at ports ‘a’ and ‘b’ given by

$$r_a[\omega_1] = \frac{\chi_a^{-1*} \chi_b^{-1} - \rho^2}{\chi_a^{-1} \chi_b^{-1} + \rho^2}, \quad (22)$$

$$r_b[\omega_1] = \frac{\chi_a^{-1} \chi_b^{-1*} - \rho^2}{\chi_a^{-1} \chi_b^{-1} + \rho^2}. \quad (23)$$

The inverse bare response functions $\chi_{a,b}^{-1}$ of modes ‘a’ and ‘b’ are given by Eq. (18).

After including the wave interference effect introduced by the 90° hybrid, we finally arrive at the following expressions for the scattering matrix of the device

$$S_{21}[\omega_1] = \frac{1}{2} (i s_{1'1'} + i s_{2'2'} + s_{2'1'} - s_{1'2'}), \quad (24)$$

$$S_{12}[\omega_1] = \frac{1}{2} (i s_{1'1'} + i s_{2'2'} + s_{1'2'} - s_{2'1'}), \quad (25)$$

$$S_{11}[\omega_1] = \frac{1}{2} (s_{1'1'} - s_{2'2'} + i s_{2'1'} + i s_{1'2'}), \quad (26)$$

$$S_{22}[\omega_1] = \frac{1}{2} (s_{2'2'} - s_{1'1'} + i s_{2'1'} + i s_{1'2'}). \quad (27)$$

To calculate the JIS transmission response versus frequency that matches the measured curves in Fig. 3 (in the main text), we evaluate $|S_{21}|^2$, $|S_{12}|^2$ based on Eqs. (24), (25), while substituting $\omega_p/2\pi = 2.727$ GHz (applied in the experiment) and $\varphi = -\pi/2$ ($\varphi = \pi/2$) when P₁ (P₂) is driven. We also substitute $\gamma_a/2\pi = 40$ MHz (measured), $\gamma_b/2\pi = 100$ MHz (set to match the bandwidths of the measured curves), and $|\alpha| = 0.51$. The latter parameter, i.e., $|\alpha|$, is evaluated by varying ρ and $|\alpha|$ to simultaneously best match one pair of $|S_{21}|^2$, $|S_{12}|^2$ values measured on-resonance for the same pump power and pump port. This is because, on resonance, the device response in both directions is solely dependent on these two parameters. Next, for each pair of curves $|S_{21}|^2$, $|S_{12}|^2$ measured for the same pump power and pump port, we substitute $\omega_a/2\pi$ corresponding to the frequency of the respective isolation dip. This is done because the theoretical model does not account for shifts in the JPC resonance frequency due to the Kerr effect. Finally, for each pair of curves ($|S_{21}|^2$, $|S_{12}|^2$ corresponding to the same pump power and pump port), we substitute ρ that gives the respective isolation dip magnitude on resonance.

One likely physical reason for the deviation of the parameter value $|\alpha| = 0.51$ in our device from $1/\sqrt{2}$ expected for an ideal symmetric coupler (in which α the coupling coefficient between the ‘b’ modes of the two JPCs is equal to β the coupling coefficient of each JPC to the cold termination, see Supplementary Figure 1a) is the presence of two coupling capacitors in series between the two JPCs, which couple the JPCs to the intermediate delay line (see the device configuration shown

in Figs. 1d,g). Having these two coupling capacitors in-series in the path between the two JPCs, instead of one, effectively reduces the coupling for wave amplitudes by $\sqrt{2}$, thus giving $|\alpha| = 0.5$, which matches well the estimated value of 0.51 in our device.

Supplementary Note 3: JPC Hamiltonian

The bare Hamiltonian of a nondegenerate three-wave mixing device, comprised of three parallel LC resonators coupled via a dispersive nonlinear medium, can be written as [1, 5]

$$H_0 = \frac{\Phi_X^2}{2L_a} + \frac{\Phi_Y^2}{2L_b} + \frac{\Phi_Z^2}{2L_c} + \frac{Q_X^2}{2C_a} + \frac{Q_Y^2}{2C_b} + \frac{Q_Z^2}{2C_c} + K\Phi_X\Phi_Y\Phi_Z, \quad (28)$$

where $\Phi_{X,Y,Z}$ are the generalized flux variables of the three resonators and $Q_{X,Y,Z}$ are the corresponding charge variables. The first six terms of H_0 represent the energy of three independent harmonic oscillators a, b, and c, having angular frequencies $\omega_{a,b,c} = 1/\sqrt{L_{a,b,c}C_{a,b,c}}$ and characteristic impedances $Z_{a,b,c} = \sqrt{L_{a,b,c}/C_{a,b,c}}$. Notably, the last term represents a trilinear mixing interaction between modes X, Y, and Z with a coefficient K .

Assuming that the angular frequencies of the three modes satisfy $\omega_c < \omega_a < \omega_b$, $\omega_c = \omega_b - \omega_a$, the resonators are well in the underdamped regime $\gamma_{a,b,c} \ll \omega_{a,b,c}$, where $\gamma_a, \gamma_b, \gamma_c$ are the corresponding photon escape rates, and $\gamma_a + \gamma_b \ll \omega_b - \omega_a$, which supposes that the envelopes of the drive signals exciting these modes are slow compared to the respective drive frequencies.

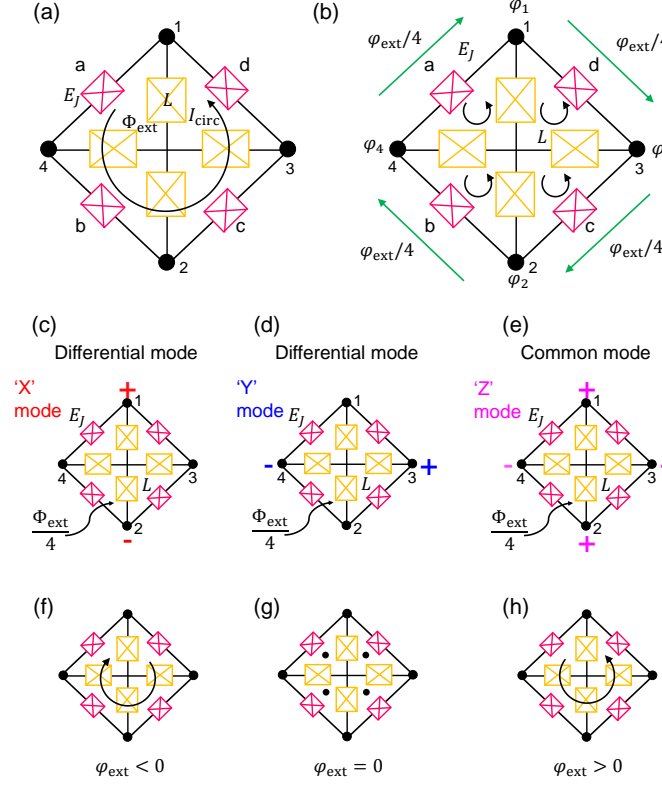
Equivalently, the Hamiltonian H_0 can be expressed in terms of bosonic operators

$$H_0 = \hbar\omega_a a^\dagger a + \hbar\omega_b b^\dagger b + \hbar\omega_c c^\dagger c + \hbar g_3 (a^\dagger + a) (b^\dagger + b) (c^\dagger + c), \quad (29)$$

where $a^\dagger, a, b, b^\dagger, c^\dagger, c$ are the raising and annihilation operators associated with the three modes, which commute with each other and satisfy the standard commutation relations $[a, a^\dagger] = 1, [b, b^\dagger] = 1, [c, c^\dagger] = 1$. The coupling constant between the modes g_3 is assumed to be much smaller than the angular frequencies $\omega_{a,b,c}$ and decay rates $\gamma_{a,b,c}$.

By further working in the framework of the rotating wave approximation and assuming a classical coherent drive (i.e., pump) at $\omega_p = \omega_c = \omega_b - \omega_a$ and $g_3 \geq 0$, we obtain

$$H_{3\text{wave}} = \hbar|g_{ab}|(e^{i\phi_p} ab^\dagger + e^{-i\phi_p} a^\dagger b), \quad (30)$$



Supplementary Figure 2: JRM structure, eigenmodes, and circulating currents. **a** The JRM consists of four Josephson junctions a, b, c, d with energy E_J , which are arranged in a Wheatstone bridge configuration between nodes 1, 2, 3, 4. The four large inner junctions, each with inductance L , function as linear shunt inductors for the JRM junctions. An externally applied magnetic flux threading the JRM loop gives rise to a circulating dc-current I_{circ} . **b** The diagram shows the reduced node fluxes $\varphi_1, \varphi_2, \varphi_3, \varphi_4$ used in the calculation of the JRM eigenmodes. The four inner loops are assumed to be equal in size, thus each loop receives a quarter of Φ_{ext} . When the JRM is biased at a primary flux lobe, no dc current flows in the shunt inductances inside the JRM (i.e., the circulating currents in the inner branches cancel each other). **c, d, e** exhibit the polarity of the rf node-voltages corresponding to the eigenmodes of the JRM. **c** and **d** show the polarity patterns for the differential excitation modes ‘X’, ‘Y’, respectively. **e** shows the pattern for the common excitation mode ‘Z’. **f, g, h** illustrate the correspondence between the circulating current direction and the sign of the reduced external magnetic flux φ_{ext} . The black discs in **g** indicate no circulating currents.

where $g_{ab} = g_3 \sqrt{\bar{n}_c} e^{-i\phi_p}$. In the derivation of Eq. (30), we replaced the annihilation operator c by its average value in the coherent state produced by the pump, where \bar{n}_c is the average pump photon number and ϕ_p is the pump phase.

To find g_3 , we express the mode amplitudes, i.e., $\Phi_{X,Y,Z}$, in terms of the corresponding bosonic

operators: $\Phi_X = \Phi_X^0(a + a^\dagger)$, $\Phi_Y = \Phi_Y^0(b + b^\dagger)$, $\Phi_Z = \Phi_Z^0(c + c^\dagger)$, where $\Phi_{X,Y,Z}^0 = \sqrt{\hbar Z_{a,b,c}/2}$ are the zero-point-fluctuations of the flux. Using these relations and Eqs. (28), (29), we obtain the following link between g_3 and K [1]

$$\hbar g_3 = K \Phi_X^0 \Phi_Y^0 \Phi_Z^0. \quad (31)$$

In the case of the JPC, the mixing term $K\Phi_X\Phi_Y\Phi_Z$ originates from the JRM, which functions as a dispersive nonlinear mixing element. As seen in Supplementary Figure 2a, the JRM consists of four nominally identical Josephson junctions with energy $E_J = \varphi_0 I_0$, i.e., a, b, c, d, arranged in a Wheatstone bridge configuration, where $\varphi_0 = \Phi_0/2\pi$ is the reduced flux quantum ($\Phi_0 = h/2e$), and I_0 is the critical current. The JJs of the JRM are shunted by linear inductors in the form of large inner Josephson junctions, each with inductance L . Externally applied magnetic flux threading the JRM Φ_{ext} , induces a dc current I_{circ} circulating in the outer loop.

For a symmetrical JRM, in which the areas of the four inner loops are equal, as shown in Supplementary Figure 2b, the external flux threading them is $\Phi_{\text{ext}}/4$ and for $0 \leq |\Phi_{\text{ext}}| \leq 1.4\Phi_0$ (i.e., located on the primary flux lobe), no dc currents flow in the inner branches. It is straightforward to show that the JRM supports 4 spatial eigenmodes, three which resonate at microwave frequencies X, Y, Z (shown in Supplementary Figure 2c,d,e) and a fourth (not shown) which is at dc [5]. As seen Supplementary Figure 2c,d,e, two of the eigenmodes ‘X’ and ‘Y’ are differential, whereas Z is a common excitation. As can be inferred from Supplementary Figure 2b-e, the reduced branch fluxes representing these eigenmodes ($\varphi'_{X,Y,Z} \equiv \Phi'_{X,Y,Z}/\varphi_0$) can be expressed as orthogonal linear combinations of the reduced node fluxes of the JRM (i.e., $\varphi_i = \Phi_i/\varphi_0$, $i = 1, 2, 3, 4$): $\varphi'_X = \varphi_1 - \varphi_2$, $\varphi'_Y = \varphi_3 - \varphi_4$, $\varphi'_Z = (\varphi_1 + \varphi_2 - \varphi_3 - \varphi_4)/2$. Since the branch fluxes across the JRM $\Phi'_{X,Y,Z}$ are only a fraction of the total generalized fluxes $\Phi_{X,Y,Z}$ of the oscillators in Eq. (28), they satisfy $\Phi'_{X,Y,Z} = p_{a,b,c} \Phi_{X,Y,Z}$, where $p_{a,b,c} \approx L_{J0}/L_{a,b,c}$ are participation ratios representing the fraction of the spatial modes contained in the JRM and $L_{J0} = \varphi_0/I_0$ is the linear inductance of the outer JJs.

For small $\varphi'_{X,Y,Z} \ll 1$, the Hamiltonian of the shunted JRM reads [5, 7]

$$\begin{aligned}
H_{\text{JRM}} = & -E_{\text{J}} \sin\left(\frac{\varphi_{\text{ext}}}{4}\right) \varphi'_{\text{X}} \varphi'_{\text{Y}} \varphi'_{\text{Z}} \\
& + \left(\frac{E_{\text{L}}}{2} + E_{\text{J}} \cos\left(\frac{\varphi_{\text{ext}}}{4}\right)\right) \left(\frac{\varphi'^2_{\text{X}}}{2} + \frac{\varphi'^2_{\text{Y}}}{2}\right) \\
& + 2 \left(\frac{E_{\text{L}}}{4} + E_{\text{J}} \cos\left(\frac{\varphi_{\text{ext}}}{4}\right)\right) \varphi'^2_{\text{Z}} \\
& - 4E_{\text{J}} \cos\left(\frac{\varphi_{\text{ext}}}{4}\right), \tag{32}
\end{aligned}$$

where $\varphi_{\text{ext}} = \Phi_{\text{ext}}/\varphi_0$ is the reduced external flux, $E_{\text{L}} = \varphi_0^2/L$ is the inductive energy of the large inner JJs. The first term of H_{JRM} is a three-wave mixing term, whereas the second and third terms are quadratic in the mode fluxes and therefore renormalize the mode frequencies. The fourth term is a constant (for a given external flux), that is independent of the mode fluxes.

To calculate g_3 we rewrite the mixing term of H_{JRM} in the format of the right-hand side of Eq. (31), which gives

$$g_3 = -\frac{E_{\text{J}}}{\hbar} \sin\left(\frac{\varphi_{\text{ext}}}{4}\right) \frac{\text{PaPbPc}}{\varphi_0^3} \Phi_{\text{X}}^0 \Phi_{\text{Y}}^0 \Phi_{\text{Z}}^0. \tag{33}$$

Finally, substituting $\Phi_{\text{X,Y,Z}}^0 = \sqrt{\hbar Z_{\text{a,b,c}}/2} = \sqrt{\hbar \omega_{\text{a,b,c}} L_{\text{a,b,c}}/2}$ in Eq. (33) yields

$$g_3 = -\sin\left(\frac{\varphi_{\text{ext}}}{4}\right) \sqrt{\frac{\text{PaPbPc} \omega_{\text{a}} \omega_{\text{b}} \omega_{\text{c}}}{E_{\text{J}}^{\text{eff}}/\hbar}}, \tag{34}$$

where $E_{\text{J}}^{\text{eff}}$ is the effectively available Josephson energy, which is proportional to E_{J} with a numerical prefactor. This result shows that (1) the sign of the coupling constant g_3 is opposite of the external flux φ_{ext} in the range $-1.4 \cdot 2\pi \leq \varphi_{\text{ext}} \leq 1.4 \cdot 2\pi$ (corresponding to the JPCs being flux-biased on the primary flux lobe), (2) the magnitude of g_3 varies with $\left|\sin\left(\frac{\varphi_{\text{ext}}}{4}\right)\right|$, for example it vanishes (no mode coupling) when $\varphi_{\text{ext}} = 0$. In Supplementary Figure 2f,g,h, we show illustrations of the direction of the dc current flowing in the JRM for $\varphi_{\text{ext}} < 0$, $\varphi_{\text{ext}} = 0$, $\varphi_{\text{ext}} > 0$, respectively, which follows the relation $\text{sgn}(\varphi_{\text{ext}}) = \text{sgn}(\text{I}_{\text{circ}})$. The black discs in Supplementary Figure 2g corresponding to $\varphi_{\text{ext}} = 0$, indicate that the circulating current is zero.

Based on Eq. (34), we can rewrite Eq. (30) in the general form,

$$H_{\text{3wave}} = \hbar |g_{\text{ab}}| (e^{i\phi'_{\text{p}}} a b^\dagger + e^{-i\phi'_{\text{p}}} a^\dagger b), \tag{35}$$

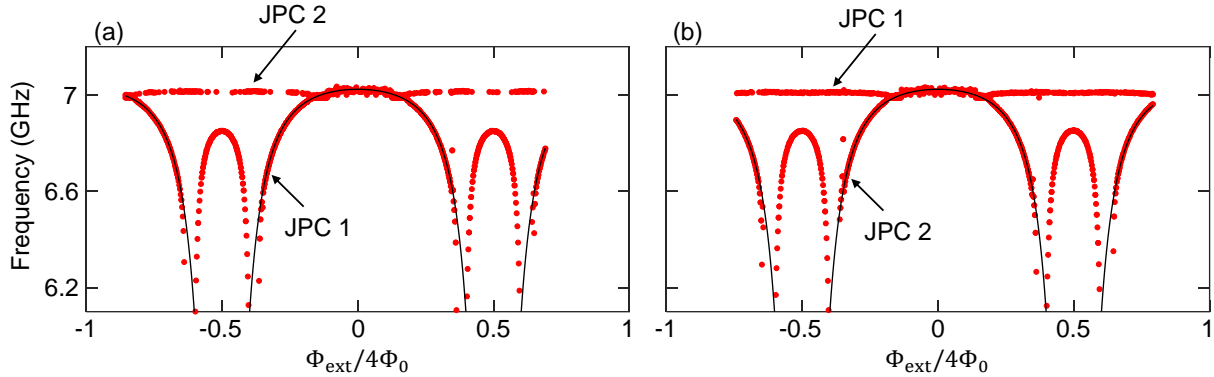
where $\phi'_{\text{p}} = \phi_{\text{p}} + n_{\text{g}}\pi$ and

$$n_g = \begin{cases} 0 & \varphi_{\text{ext}} \leq 0 \\ 1 & \varphi_{\text{ext}} > 0 \end{cases}. \quad (36)$$

Note that in the experiment, we cannot determine the sign of I_{circ} or φ_{ext} flux biasing the JPCs directly. We only know the sign of the dc current I_{coil} generated by the room-temperature current source, which biases the small superconducting coil attached to each JPC. Therefore, to determine the parity of $\varphi_{\text{ext}1,2}$, we take the following steps: (1) we make an arbitrary assumption regarding φ_{ext} of one JPC, for example $\text{sgn}(\varphi_{\text{ext}1}) = \text{sgn}(I_{\text{circ}1}) = \text{sgn}(I_{\text{coil}1})$, where $I_{\text{coil}1}$ is considered negative only if it is smaller than $I_{\text{offset}1}$, which is the dc current for which the JPC is biased at the maximum frequency of the primary flux lobe (corresponding to $\varphi_{\text{ext}1} = 0$). In general, I_{offset} is slightly off zero when there is a nonzero magnetic field within the cryoperm magnetic shield can enclosing the device. (2) We flux bias JPC₁ at $I_{\text{coil}1} < I_{\text{offset}1}$ for which we assume $\varphi_{\text{ext}1} < 0$. (3) We set $I_{\text{coil}2}$ such that it is negative, i.e., $I_{\text{coil}2} < I_{\text{offset}2}$, and aligns the resonance frequency of JPC₂ with that of JPC₁ at $I_{\text{coil}1}$. (4) We apply a pump tone to P₁ (for which $\varphi_p = -\pi/2$) and tune its frequency and power to yield a near unity transmission in one direction and isolation in the other direction. (5) Since $\text{sgn}(g_3) = -\text{sgn}(\varphi_{\text{ext}})$, the sign of g_3 of both JPCs is the same if $\text{sgn}(\varphi_{\text{ext}1}) = \text{sgn}(\varphi_{\text{ext}2})$. Thus, if we obtain in step (4) $|S_{21}| \rightarrow 1$ and $|S_{12}| \rightarrow 0$, this implies based on Eqs. (2), (3) that the sign of g_3 of both JPCs is the same (i.e., $p = 0$), otherwise the response is reversed. Lastly, (6) once we find in step (5) a pair $(I_{\text{coil}1}, I_{\text{coil}2})$ which gives rise to the same g_3 sign based on the device response, we can determine the other parity configurations in a self-consistent manner including for a pump fed through P₂.

Supplementary Note 4: JIS characterization measurements

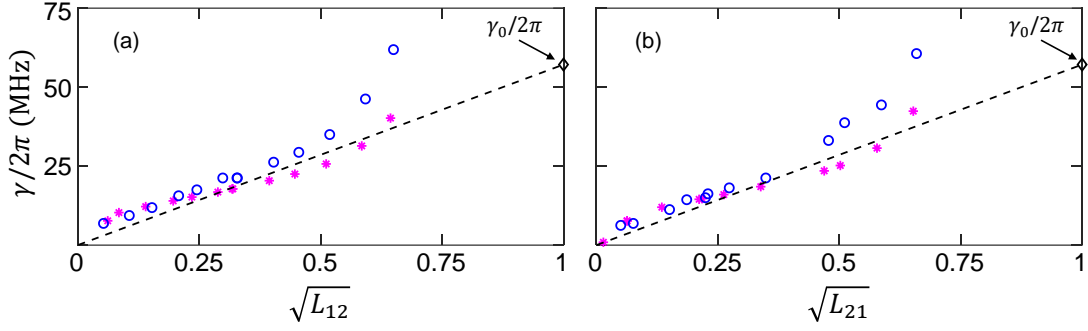
In Supplementary Figure 3a,b, we exhibit the dependence of the resonance frequency of mode ‘a’ of JPC₁ and JPC₂ on applied external flux threading the respective JRM. In Supplementary Figure 3a (Supplementary Figure 3b), the resonance frequency of mode ‘a’ of JPC₁ (JPC₂) is varied as a function of external flux applied to JRM₁ (JRM₂), while parking the resonance frequency of mode ‘a’ of JPC₂ (JPC₁) at its maximum (corresponding to a fixed applied flux threading JRM₂ (JRM₁)). The filled red circles represent measured data points, while the black solid curves represent theory fits to the major flux lobes of the JPCs. The theoretical model used to produce the fits is the same as in Refs. [7, 8]. It is worthwhile noting that both fits employ the same device



Supplementary Figure 3: JPC resonance frequency versus external magnetic flux. **a** and **b** exhibit the resonance frequency of mode ‘a’ of the two JPCs that make the JIS as a function of the external magnetic flux threading the first and second JRMs, respectively. In measurements **a** and **b**, mode ‘a’ of JPC₂ and JPC₁ is parked at its maximum frequency via a constant magnetic flux applied to JRM₂ and JRM₁, respectively. The solid black curves represent theory fits. The fits employ the same device parameters in both plots.

parameters. This suggests that fabrication variations on the same chip are small and that the JPCs are indeed nominally identical. From the fits, we extract the following device parameters: $I_0 = 2.82 \mu\text{A}$ the critical current of the outer Josephson junctions of the JRM, $f_{\text{max}} = 7.0232 \text{ GHz}$ the maximum resonance frequency of mode ‘a’, $Z_{\text{res}} = 51.1 \text{ Ohm}$ the characteristic impedance of the JPC resonators, $L_{J0}/L = 3.1$ the Josephson inductance ratio between the outer and inner JRM junctions, and $L_{J0}/L_s = 5$ the inductance ratio between the JRM outer Josephson junctions and the parasitic series inductance of the superconducting wire in each arm.

To investigate the dependence of the dynamical bandwidth of the JIS $\gamma/2\pi$ on the transmission dip in the isolated direction $L_{ij} = \min|S_{ij}|^2$, we plot in Supplementary Figure 4 using blue circles the extracted bandwidths corresponding to the frequency difference of the 3 dB points above the minimum of the measured curves (some of which are presented in Fig. 3 in the main text). We also plot using magenta stars the calculated bandwidths extracted from the theory curves. As seen in Supplementary Figures. 4a,b, in which $\gamma/2\pi$ is plotted as a function of $\sqrt{L_{12}}$ and $\sqrt{L_{21}}$, respectively, corresponding to the JIS operated in the forward $1 \rightarrow 2$ and backward $2 \rightarrow 1$ directions, the calculated bandwidths exhibit a good agreement with the measured data, especially in the limit of vanishing L_{ij} , which correspond to large isolations. This behavior mimics the shrinking bandwidths of Josephson amplifiers, such as JPAs and JPCs, in the limit of large gains due to the bandwidth-amplitude gain product, which is characteristic of resonant-structure based



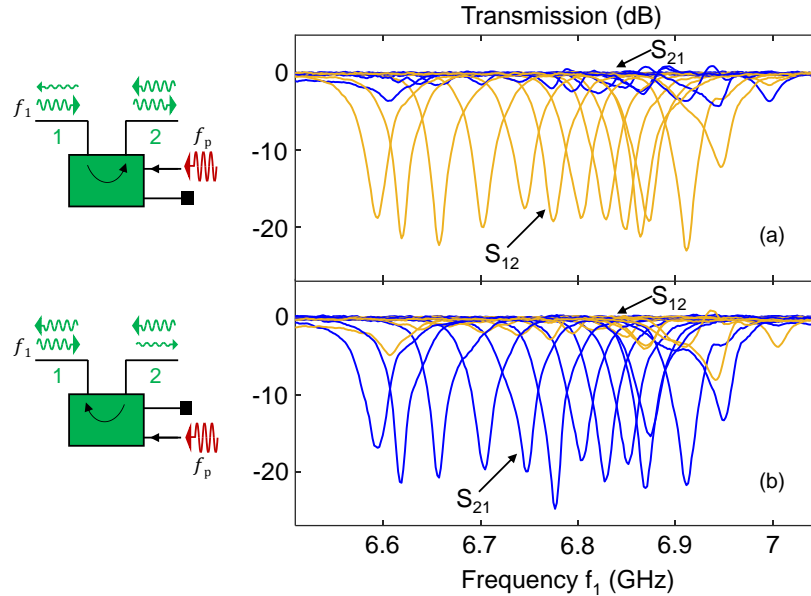
Supplementary Figure 4: Bandwidth inverse-amplitude-attenuation product measurement.

Dynamical bandwidth of JIS ($\gamma/2\pi$) versus its amplitude attenuation $\sqrt{L_{12}} = |S_{12}|$ and $\sqrt{L_{21}} = |S_{21}|$ depicted in plots **a** and **b**, respectively. The blue circles are data extracted from the measurements of Fig. 2 (in the main text) for different pump drives fed to P_1 and P_2 . The magenta stars are theoretical results extracted from the calculated curves. The black diamond corresponds the effective linear bandwidth of JIS when it is off ($L = 1$). The dashed black line corresponds to the relation $\gamma = \gamma_0\sqrt{L}$.

parametric devices [1, 9]. To highlight this observed behavior in the JIS case, we plot using black dashed line the relation $\gamma = \gamma_0\sqrt{L}$, where $\gamma_0 = 2\gamma_a\gamma_b/(\gamma_a + \gamma_b)$, indicated by a black diamond, is the effective linear bandwidth of the JPC without pump $\gamma_0/2\pi = 57$ MHz, where $\gamma_a/2\pi = 40$ MHz and $\gamma_b/2\pi = 100$ MHz.

Another related figure of merit is the tunable bandwidth of the device. In Supplementary Figure 5, we exhibit a tunable bandwidth measurement of the JIS. In this measurement, we vary the magnetic fluxes threading the two JRMs in tandem and adjust the pump power and frequency to yield isolation of more than 18 dB in the attenuated signal direction $|S_{12}|^2$ (orange curves) or $|S_{21}|^2$ (blue curves) depending on which pump port is driven, i.e., P_1 in Supplementary Figure 5a and P_2 in Supplementary Figure 5b. As seen from this measurement, the JIS possesses a tunable bandwidth of about 300 MHz in both operation modes. This bandwidth is determined by the tunable bandwidths of the two JPCs, the resonance frequency matching of both modes ‘a’ and ‘b’ as a function of applied flux, as well as the bandwidths of the on-chip 90° hybrids.

Lastly, we measure in Supplementary Figure 6 the saturation power of the JIS in the forward (plot a) and backward (plot b) directions for the working point presented in Fig. 2 in the main text. This figure of merit represents the maximum input signal power, which the device can handle for a fixed pump frequency $f_p = 2.758$ GHz and power before its transmission/isolation response increases or decreases by 1 dB. As seen in the figure, the saturation power of the JIS, indicated by

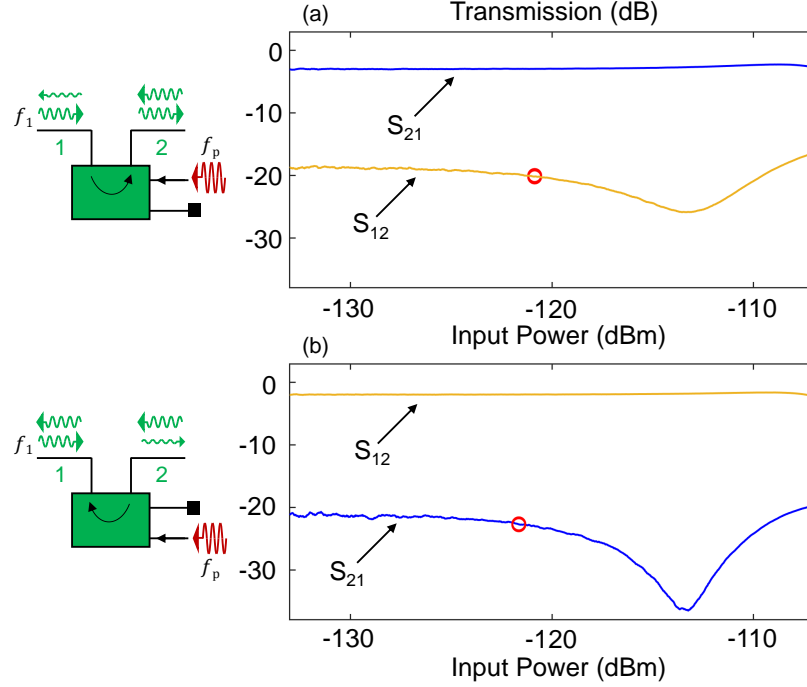


Supplementary Figure 5: Tunable bandwidth measurement. The resonance frequencies of the JPCs are varied in-tandem by varying the magnetic fluxes threading the two JRMs. For each flux working point, the pump frequency and power are adjusted to yield isolation of more than 18 dB in the relevant signal direction depending on which pump port is driven, i.e., P_1 in **a** and P_2 in **b**.

the red circles, is about -121 dBm and it is determined by a change in the isolation magnitude, which, notably, occurs at about 14 dB lower than the onset of observed change in the transmission magnitude. While this measured saturation power is smaller than the one reported in the proof-of-principle PCB-integrated JIS [4] by about 12 dB, it falls within the measured saturation power range of JPCs operated in amplification or frequency conversion [1, 2]. Since the power handling capacity of JPCs are the limiting factor in this case, we expect this figure of merit of the JIS to significantly improve as high-saturation power JPCs become available in the future.

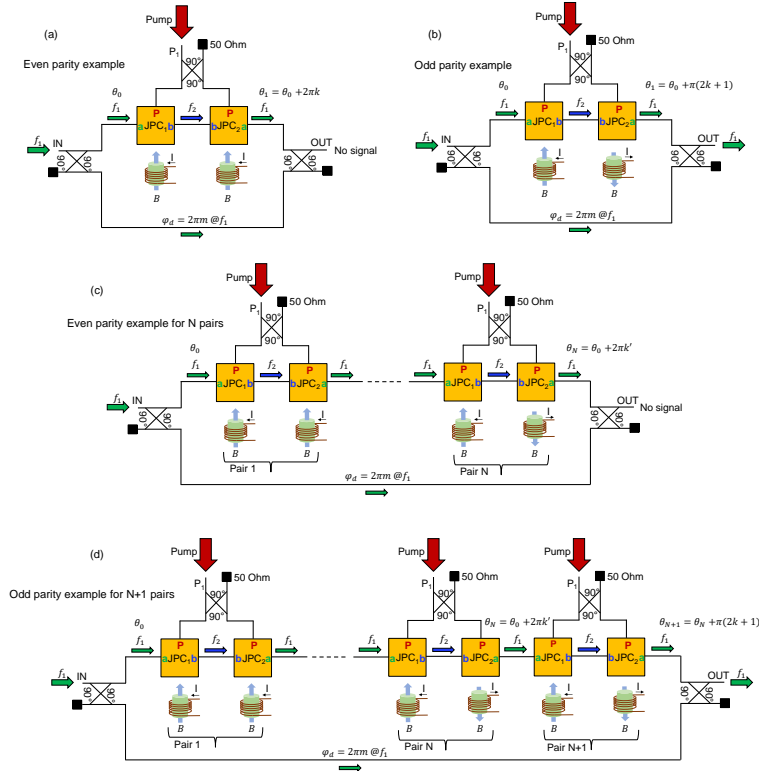
Supplementary Note 5: Orientation parity detection scheme of weak magnetic sources

As demonstrated in Fig. 4 (in the main text), the isolation direction of JIS is determined not only by the phase gradient between the pumps feeding the two JPCs but also by the parity of the magnetic fields flux biasing their JRMs. In this section, we show how this interesting property could potentially be used to detect the orientation parity of weak magnetic sources via direct microwave transmission measurements. In Supplementary Figure 7a,b, we show an exemplary detection setup that relies on this property. The setup acts as a two-path interferometer for coherent microwave



Supplementary Figure 6: Saturation power measurement of the JIS. **a** and **b**, corresponding to pump drives applied to port P_1 and P_2 , respectively, exhibit transmission parameters of the JIS, i.e., $|S_{21}|^2$ (blue), $|S_{12}|^2$ (orange), measured as a function of the signal input power. The red circles indicate the maximum input power for which the transmission magnitude of the JIS changes by 1 dB relative to the low-power value.

signals at frequency f_1 . It consists of an input and output quadrature couplers, i.e., 90° hybrids, whose inner ports are coupled through two paths. The first (top) path, incorporates a gyrator formed by two JPCs coupled via their ‘b’ mode [10]. The second (bottom) path, includes a lossless transmission line, whose electrical length is an integer multiple of the signal wavelength at f_1 . The signal frequency f_1 used in the scheme lies within the bandwidth of mode ‘a’ of the JPCs. The two JPCs are operated in frequency conversion mode without photon gain, i.e., signals entering port ‘a’ (‘b’) are transmitted to port ‘b’ (‘a’) with frequency conversion, and driven through a dedicated 90° hybrid using a single pump drive, whose frequency is set to $f_p = f_2 - f_1$, where f_2 lies within the bandwidth of mode ‘b’. Assuming, without loss of generality, that the pump driving the gyrator is fed through port P_1 of the hybrid ($\varphi_p = -\pi/2$), the microwave signals transversing the gyrator acquire a differential phase, i.e., $2\pi k$ or $(2k + 1)\pi$, $k \in \mathbb{Z}$, depending on the propagation direction of the signals (i.e., from JPC_1 to JPC_2 or vice versa) and the direction



Supplementary Figure 7: Parity detection schemes of the orientation of weak magnetic sources.

a and **b** depict interferometers formed by two 90° hybrids, which interfere waves propagating in two paths, i.e., top and bottom. The top path includes a pair of JPCs coupled back-to-back via their ‘b’ mode. The two JPCs are operated in full frequency conversion mode. They are driven by a single pump tone, which is fed through a third 90° hybrid that couples to the pump ports of the JPCs. The bottom path includes a lossless delay line, which adds an integer number of wavelengths at f_1 . The scheme measures the transmission of a probe signal at f_1 input on the IN port of the left hand-side hybrid and output at the OUT port of the right hand-side hybrid. Minimum or maximum transmission through the device, resulting from respective destructive and constructive wave interference, is obtained if the orientation parity of the magnetic fluxes flux-biasing the JPCs is even **a** or odd **b**. **c** A generalized detection scheme for N pairs of magnetic sources, which flux-bias N pairs of JPCs that are incorporated into the top path. The scheme response is illustrated for the case of an even parity. **d** An extended version of the scheme in **c** with a total of $N+1$ pairs of JPCs and magnetic sources in the top path. In this case, the scheme response is illustrated for an odd parity measurement.

parity of the magnetic fields flux-biasing the JPCs, as illustrated in Supplementary Figures 7a,b. If we further restrict ourselves, for simplicity, to transmission measurements of signals entering the upper external port of the left 90° hybrid and exiting via the upper external port of the right

90° hybrid, we obtain zero transmission (no output signal, ‘0’) in the case of even parity of the biasing magnetic fields (Supplementary Figure 7a) and unity transmission (an output signal, ‘1’) in the case of odd parity of the biasing magnetic fields (Supplementary Figure 7b). In the former (latter) case, the zero (unity) transmission is the result of a destructive (constructive) interference between waves propagating in the upper and bottom paths of the interferometer, which accumulate opposite (equal) phases.

It is important to point out that this proposed magnetic field parity detection scheme is not limited to two magnetic sources. It can be applied to N pairs of weak independent magnetic sources as shown in Supplementary Figure 7c, which flux bias N gyrators incorporated in series into the upper path of the interferometer. To prove the validity of this generalization, we apply the induction method. The first (base) step of the proof, in which we demonstrate the validity of the measurement setup for a given N , is shown in Supplementary Figures 7a,b for the case $N=1$. In the second (inductive) step, we demonstrate that the detection scheme is valid for $N+1$ pairs, given that it is valid for N , as partially illustrated in Supplementary Figure 7d. To do that we consider four different cases:

Case 1: the first N pairs of magnetic sources have an even number of aligned magnetic fields and the two magnetic fields biasing the $(N+1)$ th gyrator are aligned in the same direction (i.e., have an even parity as well). Since the parity detection scheme works for the first N pairs (resulting in a destructive interference at the output), this means that the accumulated phase of the transmitted signal via the upper path is $\theta_N - \theta_0 = 2\pi k'$. By adding the $(N+1)$ th pair having an even parity (similar to the case of Supplementary Figure 7a), the total accumulated phase at the output of the $(N+1)$ th pair is given by $\theta_{N+1} - \theta_0 = 2\pi k''$, where $k'' = k + k'$ and $k, k', k'' \in \mathbb{Z}$. Since the bottom path always yields an accumulated phase of $(2m + 1)\pi$, where $m \in \mathbb{Z}$, the waves propagating in the upper and bottom paths will destructively interfere at the output, thus confirming that the setup is valid for $N+1$ pairs in this case.

Case 2: the first N pairs of magnetic sources have an even number of aligned magnetic fields and the two magnetic fields biasing the $(N+1)$ th gyrator are aligned in the opposite directions (i.e., have an odd parity), which means that the $N+1$ pairs have odd parity in total. By concatenating the $(N+1)$ th pair having an odd parity (similar to the case of Supplementary Figure 7b), the total accumulated phase at the output of the $(N+1)$ th pair is given by $\theta_{N+1} - \theta_0 = (2k'' + 1)\pi$. Consequently, the waves propagating along the upper and bottom paths will constructively interfere at the output (indicating an odd parity of the whole chain), thus confirming that the setup is valid for $N+1$ pairs in this case as well.

Case 3: the first N pairs of magnetic sources have an odd number of aligned magnetic fields and the two magnetic fields biasing the $(N+1)$ th gyrator are aligned in the opposite directions (i.e., have an odd parity). This means that the $N+1$ pairs have even parity in total. It is straightforward to show that the total accumulated phase at the output of the $(N+1)$ th pair is $\theta_{N+1} - \theta_0 = 2\pi k''$, which yields a destructive interference (no signal) at the device output, which is indicative of even parity.

Finally, the fourth and last case is similar to case 3 except that the $(N+1)$ th gyrator is flux biased with two aligned magnetic fields (i.e., having an even parity as in Supplementary Figure 7a). In this case, the whole chain ($N+1$ pairs) will preserve the odd parity of the N pairs. Since the total accumulated phase at the output of the $(N+1)$ th pair is given by $\theta_{N+1} - \theta_0 = (2k'' + 1)\pi$, the resultant wave interference at the output of the device is constructive, which, in turn, yields an output signal indicative of odd parity.

Such interferometric microwave detection schemes could potentially be used in a variety of applications. For example, they can be used to perform a Z operator parity checks on flux qubits or capacitively shunted flux qubits (CSFQs) using direct microwave transmission measurements (as opposed to (1) using ancilla qubits coupled to data qubits, (2) entangling them via single- and two-qubit gates, and (3) measuring the final state of the ancilla qubits as done in the surface code architecture). In such an application, each CSFQ is coupled to a JRM via a suitable mutual inductance. Since the qubit state is encoded in the direction of the persistent current in the CSFQ loop, opposite circulating currents would introduce opposite magnetic flux biases through the JRM, which would determine the transmitted signal through the interferometric device based on the parity of the qubit states. As another example, they can be used to determine the strength and orientation of weak magnetic sources. This can be done by (1) coupling the source of the unknown magnetic field to one JRM of the interferometric gyrator device, (2) flux biasing the other JRM using a controlled and well-characterized magnetic field, (3) injecting a pump tone to either P_1 or P_2 , (4) applying a microwave signal to the device input, and (5) maximizing the transmitted microwave through the device by varying the power and frequency of the applied pump as well as the magnetic field of the controlled magnetic source. For a pump tone applied to P_1 , for example, a maximum output signal is expected when the two magnetic fluxes threading the two JRMs have equal magnitudes but opposite signs (as seen in Supplementary Figure 7b).

We can estimate the range of magnetic fields B_{ext} that are typically applied to JRM loops of area A at the JRM plane, by considering the bounds $0.1\Phi_0/A < |B_{\text{ext}}| < \Phi_0/A$. For a JRM loop area of $A = 100 \mu\text{m} \times 100 \mu\text{m}$, the range is $2 \cdot 10^{-8}\text{T} < |B_{\text{ext}}| < 2 \cdot 10^{-7}\text{T}$. Much smaller field bounds

can be detected using a larger loop. However, bigger loops could add series linear inductance to the JRM, which is undesired (especially when it is comparable to the Josephson inductance of the JJs).

-
- [1] Abdo, B., Kamal, A. and Devoret, M. H. Nondegenerate three-wave mixing with the Josephson ring modulator. *Phys. Rev. B* **87**, 014508 (2013).
 - [2] Abdo, B. et al. M. Full coherent frequency conversion between two propagating microwave modes. *Phys. Rev. Lett.* **110**, 173902 (2013).
 - [3] Pozar, D. M. *Microwave Engineering*, 3rd edn (Wiley, Hoboken, 2005).
 - [4] Abdo, B. et al., Active protection of a superconducting qubit with an interferometric Josephson isolator. *Nat. Commun.* **10**, 3154 (2019).
 - [5] Schackert F. D. O. *A Practical Quantum-Limited Parametric Amplifier Based on the Josephson Ring Modulator*. Ph.D. thesis (Yale University, 2013).
 - [6] Ku, H. S. et al. Design and testing of superconducting microwave passive components for quantum information processing. *IEEE Trans. on Appl. Supercond.* **21**, 452 (2010).
 - [7] Roch, N. et al. Widely tunable, nondegenerate three-wave mixing microwave device operating near the quantum limit. *Phys. Rev. Lett.* **108**, 147701 (2012).
 - [8] Abdo, B., Chavez-Garcia, J. M., Brink, M., Keefe, G. and Chow, J. M. Time-multiplexed amplification in a hybrid-less and coil-less Josephson parametric converter. *Appl. Phys. Lett.* **110**, 082601 (2017).
 - [9] Abdo, B., Schackert, F., Hatridge, M., Rigetti, C. and Devoret, M. Josephson amplifier for qubit readout. *Appl. Phys. Lett.* **99**, 162506 (2011).
 - [10] Abdo, B., Brink, M., Chow, J. M., Gyration operation using Josephson mixers. *Phys. Rev. Applied* **8**, 034009 (2017).